Optical Fiber Microstructures for Self-Contained Whispering Gallery Mode Excitation

Michael Fraser

Dissertation submitted to the Faculty of the
Virginia Polytechnic Institute and State University
in partial fulfillment of the requirements for the degree of

Doctor of Philosophy
in
Electrical Engineering

Anbo Wang, Chairperson
Yong Xu
Yizheng Zhu
Gary R. Pickrell
Hans Robinson

March 25, 2016
Blacksburg, Virginia

Keywords: Resonators, Whispering Gallery Modes, Fiber Optics Sensors,
Micro-devices, Micro-fabrication, Wet Chemical Etching

Optical Fiber Microstructures for Self-Contained Whispering Gallery Mode Excitation

Michael Fraser

Abstract

Optical resonators, which confine light by resonant recirculation, serve as the basis for a wide variety of optical components. Though they appear in many geometric forms, the most effective of optical resonators show axial symmetry in at least one dimension. A popular variation that finds broad application is the dielectric sphere. Acclaimed for their high quality (Q) factor and small modal volume, spheres owe credit of these attractive features to their support of whispering gallery mode (WGM) resonances. The sensitivity of a resonance's frequency and Q to strain, temperature, and other parameters of the surrounding medium can be the basis for ultracompact modulators and sensors.

Physically, WGMs are special optical modes which can be understood as light rays that orbit the equator of the sphere guided by total internal reflection. Like a smooth stone can be skipped along the surface of a pond, light can be confined to the inside of a sphere by successive reflections. To best excite WGMs, the source light should initially trace a line tangent to the sphere's circumference. But incorporating a tiny sphere with such nanometric tolerances into a practical

sensor structure has its challenges and the prospects for microsphere applications have suffered because of the plight of this problem.

The work in this dissertation details the fabrication and function of three new "press fit" spherical resonators. These etched fiber micro-devices were developed to meet the demand for a robust, self-integrated means of coupling light between an optical fiber and WGMs in a microsphere resonator. The etching processes have been tuned to enable secure storage of a microsphere while also providing efficient excitation and interrogation of WGMs. Furthermore, the methods have been designed to be staightforward, quick, and repeatable. Using standard etchants on common polarization-maintaining fiber with readily purchased microspheres, the press fit resonators demonstrated here can be batch-fabricated and assembled. The press fit spherical resonator offers an alignment-free and conveniently pig-tailed WGM coupler that has great potential for bio-science sensing applications and studies of resonant bispheres.

Acknowledgments

Photonics is equal parts electronics and optics – a bustling and complex intersection of subdisciplines for which one needs a lot of help to navigate. In this regard, the mixture of bright and enthusiastic people I have met and worked with at the Center for Photonics Technology made all the difference.

I am grateful to my advisor Dr. Anbo Wang for putting such a talented team together and giving me the freedom to pursue my own research interests. My other committee members provided expert counsel and criticism that improved the quality of this work. My contact and conversations with Dr. Yong Xu and Dr. Hans Robinson gave me critical insight regarding whispering gallery modes and Mie theory respectively. Dr. Yizheng Zhu's words and dissertation work demonstrated to me the value of directing sensor designs toward batch fabrication. The meetings shared with Dr. Pickrell always drove me to think more deeply about the composition and properties of materials that can affect a design.

On the academic side, I have had the privilege of learning from some truly outstanding professors. Some personal standouts for me were Dr. Tim Pratt, Dr. Wayne Scales, and Dr. Ahmad Safaai-Jazi. Dr. Tim Pratt taught me radar systems design and digital communication systems design and he did so with an amusingly practical bent and posh British accent. My positive experiences in undergraduate electromagnetics classes with Dr. Wayne Scales convinced me to pursue the discipline in graduate school. Now Dr. Scales' upper level classes in

GPS theory and receiver design are having a similar influence on me perhaps now for my career interests. My time in Dr. Safaai-Jazi's class covering waveguides stressed correct practice and mastery of theory, while my role as his teaching assistant for electromagnetics and continuous and discrete systems re-emphasized the importance of attention to detail.

I extend my sincere thanks to all my friends and colleagues at Virginia Tech and the CPT for their support both in and outside the lab: Jiajun Wang, Ken Daengngam, Alex Kim, Terry Ong, Cheng Ma, Evan Lally, Bo Dong, James Gong, Dorothy Wang, Kathy Wang, Georgi Ivanov, Tyler Shillig, Angelo Yu, Aram Lee, Baigang Zhang, Tony Jia, Kieth DePew, Di Hu, Li Yu, Amiya Behera, Yunbin Song, Bo Liu, Zhipeng Tian, Lingmei Ma, Chennan Hu, Dian Fan, Qiang Yu, Xiaohua Lei, Haiwei Fu, Scott Zhang, Alan Overby, Zhihao Yu, Peng Lu, Ruohui Wang, Mohammad Al-Mamum, Brennan Thews, Haifeng Xuan, Jiaji He, Shuo Yang, and Peter Gartland.

I am thankful for administrative assistance from the capable staff at the Bradley Electrical and Computer Engineering Department and Physics Department. Special thanks goes to Cindy Hopkins who took me most of the way, Mary Brewer for help with final odds and ends, and Betty Wilkins for finding me a spot as a physics TA when I needed it most.

I would not have come this far if my family did not nurture my interests in science in engineering. Thank you Dad for showing me about the workshop when I was young. Not only did I learn how to hammer a nail, drill a decent hole, and

use a hacksaw, but I also picked up on the joy of design and building something for myself. For some reason, ambitious projects often create loud noises and large messes. Thank you Mom for putting up with all that and encouraging me all the same. Thank you to my sister Nalani for reminding me to take a break every once in a while. Thank you also to my granny Barbara Kwock for being "my pal" and always lending a friendly ear. Even when separated by thousands of miles, I appreciate all your support.

There is one special person that has walked this path beside me no matter how sharp the bend or steep the climb. Between my PhD in electrical engineering and hers in Physics, we experienced a lot of the same hardships. Through all the bad samples, ambiguous results, and broken equipment, you and I braved it all. When things worked alright, we celebrated. When things failed, we braced each other to begin again. Thank you Jeong-Ah Lee for sharing this journey, a love, many laughs, and a deep perspective that helped carry me through this PhD.

Contents

List of Figures

Chapter 1

Introduction

1.1 Background

The whispering gallery mode (WGM) resonance is a morphology-dependent phenomenon. First observed in acoustic form, the most famous example of a WGM is found at St. Paul's Cathedral in London. Apart from being ornately beautiful, its iconic dome is known to host a curious acoustic effect where whispers spoken near its walls can be heard all around its 97-meter periphery. More than a century ago, Lord Rayleigh developed a resonant wave theory to explain the effect and in so doing coined the phrase "whispering gallery" modes (WGMs) [1]. His published studies record an insightful suggestion that similar modes for an electromagnetic field might find useful applications for their extreme confinement [2, 3]. However, some time would pass before electromagnetic WGMs would be practical. Knowledge about the nature of WGMs would have to progress before

electromagnetic WGMs could be realized and their properties fully appreciated.

In recent years, optical WGMs have accumulated much attention due to their attractive potential to realize microlasers [4, 5], narrow filters [6], high resolution spectroscopy, optical switching [7], miniature biosensors [8, 9], and more. The observation of optical WGM resonances was first reported by Garrett *et al.* [10] at Bell Labs in 1961. Using a high-pressure xenon flashtube to excite spherical CaF_2 particles doped with Sm^{++}, they witnessed bright emission circling the surface of spheres provoked by the high-intensity illumination. Research advanced to incorporate WGMs with optical fibers when Stokes and Chodorow [11] of Stanford University produced the first all-fiber-ring device which combined a single-mode optical fiber and a directional coupler. By 1987, Braginsky and Ilchenko [12] had begun their studies of fused-silica microspheres with high-Q WGMs. They continued experiments into the cavity quality factor (Q-factor) and nonlinear properties of optical WGMs in specially-coated dielectric spheres [13]. In particular, their study of WGMs in high-purity fused-silica microspheres produced a record-breaking quality factor. By exciting a sphere at $633nm$, the recorded energy damping curve yielded an astounding Q factor of $(0.8\pm0.1)\times10^{10}$) [14]. The observation of this Q value was tantalizingly close to the theoretical limit imposed by fundamental material attenuation measured in optical fibers as $\sim 7\,dB$ ($5\,dB$ from bulk Rayleigh scattering and $2\,dB$ from absorption). The success of this and other experiments added to the swelling potential of WGMs for applications outside the laboratory.

By the early 1990s, optical WGM resonance devices were becoming better known for their high quality factor, high finesse (F), and very small mode volumes. Furthering the trend toward device integration, researchers started to apply micro- and nano-fabrication techniques to produce optical WGM resonators. For example, the WGM microlaser, which has a very narrow bandwidth and requires relatively low pumping power, is being aggressively pursued and may likely develop into an ideal light source for on-chip integrated optical systems. The pioneering effort of Slusher's group at Lucent, Murray Hill, created a new class of semiconductor lasers when they built the first WGM-based 3~10pm-diameter microdisk laser using selective etching techniques in InP/InGaAsP [15, 16]. Zhang *et al.* [17, 18] created InGaAsP photonic-wire microcavity ring lasers on a traditional semiconductor wafer. In the 2000s, Vahala's group at Caltech did a series of important studies on WGM microlasers in which they developed a fiber-coupled microsphere laser [4, 5], ultra-high-Q toroid microlaser [19, 20], and Raman microlaser [21, 22]. The tremendous Q factor accessible to WGMs makes them very useful, not only for high performance laser devices, but also for highly sensitive sensor applications.

Biomedicine has an abundant and pressing need for highly sensitive techniques to detect biological particles. In common practice, standard spectroscopic methods [23] are applied to detect various biological materials with great sensitivity and specificity, but are unsuitable for circumstances outside of a laboratory environment. Therefore, inexpensive, robust, and integrated devices are greatly needed

for field use. Integrated optics and photonics promise the means for opto-biological interactions in compact and hardy geometries without prohibitive expense. In recent years, the properties of WGM resonators of miniature size, small modal volume, high energy storage, and high sensitivity have been leveraged for probing biomolecules.

In 2001, Blair and Chen [24] applied the optical WGM resonances of a cylindrical microcavity for evanescent fluorescence biosensing. Binding of a labeled analyte was performed using a biospecific monolayer. The long photon lifetime of WGMs dramatically enhances absorption quantum efficiency, leading more input optical power to be absorbed by fluorophores and re-emitted as fluorescent light. The sensor showed an order of magnitude improvement in sensitivity accompanied by a sample volume reduction by many orders of magnitude. Also keen to apply optical WGM resonances towards biosensing, Boyd and Heebner [25] explored the feasibility of a biosensor design based on WGM-enhanced absorption of a biological material. They put forward a theoretical model for the sensor which estimated its sensitivity to detect as few as 100 molecules. This was followed by development of a sensitive WGM microdisk biosensor based on GaAs/AlGaAs nanofabrication techniques [8]. As with the previous approach, this sensor also detected labeled biomolecules. Convenience and ease of use naturally also drove interest toward unlabeled detection strategies.

At NYU, Arnold's research group demonstrated a number of optical biosensors for detecting unlabeled molecules [26, 27]. They used an etch-eroded optical fiber

taper coupled to a reflowed silica glass microsphere. When molecules are adhered to the surface of microsphere, resultant changes in the sphere's effective diameter and the refractive index of the surrounding environment cause a detectable shift in WGM resonance frequency. Experiments demonstrated the quantify the thickness and surface layer of an absorbed layer of bovine serum albumin adsorbed on a proper silane-functionalized microsphere [28]. Using a perturbation approach [29, 30, 31], they analyzed the resonance shift and predicted its inverse proportionality to the microsphere radius and direct proportionality to protein surface density and excess polarizability.

Researchers including Vollmer and others have continued this direction of highly sensitive whispering gallery mode resonator biosensors to demonstrate DNA detection [32, 33, 34, 35], virus particle detection [36, 37], biosensor arrays [38], and real-time reaction kinetics [39, 40, 41]. The highly sensitive and label-free operation of WGM sensors guarantees their future development and refinement. Lab-on-a-chip formats and evolved coupling techniques are expected to bring new miniaturized sensor designs out of the laboratory into hand-held, portable devices poised to perform.

1.2 Motivation

Mounting interest into microsphere resonators has fueled a growing body of important optical research. With their unique pairing of high quality factor and

submillimeter dimensions, the potential uses of microsphere resonators cover many areas. Applications have appeared in cavity quantum electrodynamics [42, 43, 44], laser stabilization [45, 46], microlasers [5, 4, 47, 48], nonlinear optics [13, 49, 50], and evanescent-wave sensing [51, 52, 53, 54, 55, 56]. Yet despite this strong overall showing, the prospects for microsphere resonator applications have suffered from the lack of a simple, fiber optic coupler [57]. To meet this demand, a small number of couplers compatible with fiber optic equipment have been proposed. There are two-sided variations such as the side-polished fiber [58, 59] and bi-conical taper [60, 61] as well as one-sided variations like the angle-polished fiber [57] and conical taper [62]. More recent coupling designs have put spheres inside or at the tip of special microstructured fibers [51, 63, 64, 65, 66]. However, all these approaches to couplers have issues that curtail their impact and widespread adoption. Polished fiber couplers are time-consuming and tedious to make. Stretched-fiber taper couplers are extremely fragile and easily contaminated. Couplers that require uncommon microstructured fibers are over-specialized and inconvenient. The key to a new and productive form of fiber optic microsphere coupler, which addresses both device integration and coupling alignment, is to design a coupling geometry using familiar, quick, and repeatable fabrication methods on materials readily at-hand. Therefore, the aim of this dissertation is to explore the feasibility of pigtailing the whispering gallery mode by integrating a microsphere inside an optical fiber while also maintaining efficient excitation.

1.3 Dissertation outline

The following is an outline of the content and significance of this dissertation:

This chapter begins with a provision of background material. The importance of coupling between waveguides and resonators is discussed and critical coupling is described using a ring resonator model. Fiber-compatible couplers including the prism coupler, angle-polished fiber, and fiber taper are covered. A geometric optics model for WGMs is mined for convenient definitions of common resonance parameters. The fundamentals of electromagnetic theory are laid out and the properties of evanescent waves are discussed.

Chapter 2 starts by outlining a derivation of standard Mie theory using definitions for spherical harmonics. Series solutions to electromagnetic fields, boundary conditions, and expansion coefficients are all covered. Efficiency factors for scattering and extinction are described as well as those defined for the near field. The source of spectral resonances is explored in the context of the multipole expansion. Morphological dependencies of the resonances on the index of the surrounding medium and absorption in the sphere are investigated. Lastly, a model for evanescent excitation of a sphere is considered. Scattering and near field efficiencies are compared for an incident plane wave versus an evanescent wave generated by different incidence angles.

Chapter 3 describes the fabrication methods for three novel press fit resonators. Etching of optical fibers is discussed generally first, before introducing ideas

regarding individual designs. Procedures are given for etching press fit resonators from three types of polarization-maintaining fiber (PMF): bow-tie fiber (BTF), reduced cladding panda fiber (RC-PMF), and standard cladding panda fiber (SC-PMF). Accompanying optical images are provided for different steps of each fabrication routine from etching to the insertion of microspheres.

Chapter 4 collects experimental results for each press fit resonator previously described. The test setup for reflection measurement is explained. Spectra are presented for each press fit resonator while submerged in isopropanol (IPA) and deionized (DI) water. Free spectral ranges (FSRs) and quality (Q) factors are observed.

Chapter 5 provides a preview of the sensing capability of the SC-PMF press fit resonator. The sensor is used to probe different concentration glucose solutions. The resonance shift in response to different surrounding index is recorded for which sensitivity and linearity are presented. Cross-sensitivity with respect to temperature is also investigated. Controlled chilling and heating of the press fit resonator are demonstrated. Peak tracking is performed and the thermal response is characterized over a 50°C range.

Chapter 6 draws conclusions and proposes future work.

1.4 Coupling

Coupling light efficiently to microresonators is a basic performance issue in photonics. Not only must a resonator be made with low loss, but a way to send and retrieve light to and from the device has to be established. Critical coupling is a prerequisite for the most efficient energy exchange. A fundamental concept in RF engineering [67], it has been recently applied to optical WGM resonators. Unlike lossless Fabry-Perot resonators where intrinsic loss and coupling loss are identical, the degree of evanescent wave coupling to WGM resonators is independent of their intrinsic loss [68]. Criticality implies that the coupling strength between waveguide and resonator must match any other losses to have 100% resonant energy exchange.

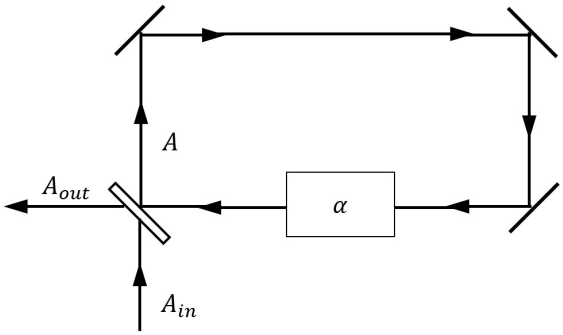

Figure 1.4.1: Ring resonator model of WGM resonator

To illustrate this, consider the model for a solid state WGM resonator as a ring cavity having a linear absorber on side [69]. At steady state, we find the intracavity field A at steady state as

$$A = A\exp(\frac{i\omega Ln}{c})\exp(-\alpha)\sqrt{1-T_c} + \sqrt{T_c}A_{in} \tag{1.4.1}$$

where $\alpha \ll 1$ and A is the (non-dispersive) total amplitude absorption of the light in the resonator per round trip, $T_c \ll 1$ is the coupling factor, $L = 2\pi R$ is the circumference of the resonator with radius R, A is the slow amplitude operator of the intracavity light, and n is the refractive index of the material. 1.4.1 indicates that steady state of the field amplitude is achieved by compensating the round trip loss of the external optical pumping A_{in}. The output pump light amplitude A_{out} can be found from

$$A_{out} = -A\exp(\frac{i\omega Ln}{c})\exp(-\alpha)\sqrt{T_c} + A_{in}\sqrt{1-T_c} \tag{1.4.2}$$

Written another way

$$A_{out} = \frac{\sqrt{1-T_c} - \exp(\frac{i\omega Ln}{c})\exp(-\alpha)}{1-\exp(\frac{i\omega Ln}{c})\exp(-\alpha)\sqrt{1-T_c}} \tag{1.4.3}$$

New notation is developed for convenience where

$$\begin{gathered} \gamma = \frac{\alpha c}{Ln}, \gamma_c = \frac{T_c c}{2Ln} \\ \frac{\omega Ln}{c} = (\omega - \omega_0) + 2\pi L \\ 2\pi L = \frac{\omega_0 Ln}{c} \end{gathered} \tag{1.4.4}$$

and ω_0 is the mode frequency and l is the mode number. Thus, near resonance

$$A_{out} = \frac{-(\gamma_c - \gamma - i(\omega_0 - \omega))}{(\gamma_c + \gamma + i(\omega_0 - \omega))A_i n} \tag{1.4.5}$$

1.4.5 shows that $\gamma = \gamma_c$ leads to $A_{out} = 0$ so that all power is absorbed in the resonator. This describes the condition of critical coupling.

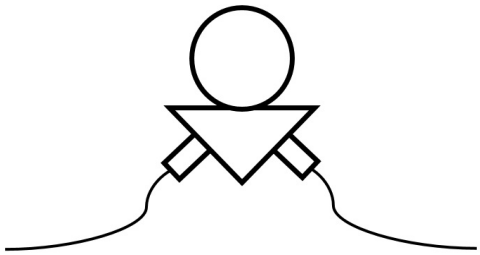

Figure 1.4.2: Prism coupler schematic

1.4.1 Prism coupler

Prism coupling was originally developed to excite optical waveguides [70, 71, 72] and has demonstrated a coupling efficiency more than 90% [30]. Studies of prism coupling to WGMs have followed, both theoretical and experimental studies [73, 74], achieving a coupling efficiency approaching 80% [75]. The approach of prism coupling observes three main principles. First, the input beam is focused into the prism at an angle to ensure phase matching between the evanescent portion of the total internally reflected wave and the WGM. Second, the beam shape is tailored to maximize the modal overlap in the near field. And third, the gap distance between the prism and resonator is controlled for critical coupling.

The prism coupler is shown schematically in Figure 1.4.2. A single mode fiber output is collimated and focused onto the prism surface. The prism is situated in close proximity to the WGM resonator and the collimated beam is focused at the contact point of the prism and resonator. Phase matching and aperture matching are important factors for efficient coupling. Coupling depends on the design materials and dimensions of both the prism and resonator as well as mutual light

interaction angles. Coupling can be controlled to a degree by varying the physical parameters, but for spherical WGM resonators, it is generally impossible to satisfy both phase-matching and aperture-matching requirements. This explains why the best achieved microsphere coupling is about 80% [75]. Coupling can be improved by varying both the incidence angle and another parameter. A popular approach is to alter the resonator's vertical radius of curvature to construct a toroidal resonator. Coupling efficiency is also affected by intermodal mixing. Larger resonators have larger modal volumes that cause competing WGMs to overlap and interact. The mode of interest can emit into other modes reducing the maximum achievable coupling. Shaping can suppress this effect by reducing the total modes and opportunities for mixing. However, even in multimode resonators, excellent coupling efficiency is possible for particular resonances that escape mixing.

1.4.2 Angle-polished fiber coupler

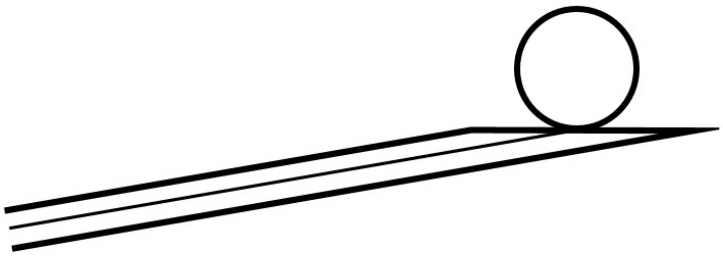

Figure 1.4.3: Angle-polished fiber coupler schematic

Angle-polished fibers provide another means for coupling light into WGM

resonators. Originally, side-polished fiber couplers [58] had limited efficiency due to residual phase mismatch between the guided wave and WGMs. Angle-polished fiber couplers present a phase-matched coupling technique in which the core-guided wave undergoes total internal reflection [57]. The essence of angle-polished fiber coupling is shown in Figure 1.4.3. The end of a single mode fiber is polished at a steep angle. Core-guided light undergoes total internal reflection at the polished face and escapes the fiber. Energy exchange between the waveguide mode of the fiber and a WGM occurs at resonance when the resonator is positioned in range of the evanescent field of the polished fiber. The angle is chosen to fulfill the phase-matching requirement. The system is generally equivalent to the prism coupler without focusing optics [57]. Note the use of this technique is limited by the availability of fibers with high refractive index.

1.4.3 Fiber taper coupler

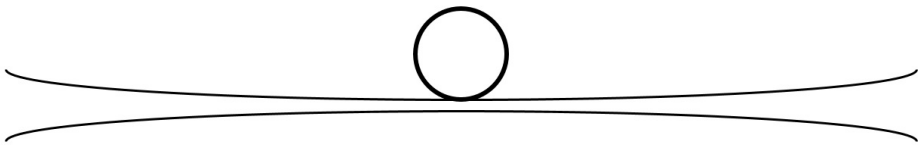

Figure 1.4.4: Fiber taper coupler schematic

Tapered fiber couplers, as depicted in Figure 1.4.4, are the most efficient of coupling schemes [75]. A fiber taper is a single mode bare waveguide of optimized diameter which for infrared wavelengths is just a few microns. The taper straddles

the resonator perimeter allowing simple input light focusing and alignment as well as output light collection. The reduced taper diameter rejects modes other than the fundamental mode. The efficiency of this scheme reaches 99.99% for fused silica resonators [61, 75]. On the downside, fiber tapers are unclad, fragile, and susceptible to contamination. They are useful for coupling to resonators with refractive indices similar to silica (~1.4-1.45) but are generally less compatible with higher index glass and crystalline resonators. Taper diameter and refractive index both affect the phase velocity. The diameter and effective refractive index gradually decrease along the same direction. Optimal placement of the resonator near the taper is necessary to achieve phase matching and critical coupling. In practice, the technique is limited by available fibers since the effective refractive index of the taper occurs between the value of the fiber material's refractive index and that of the surrounding medium be it air or vacuum.

1.5 Geometric model

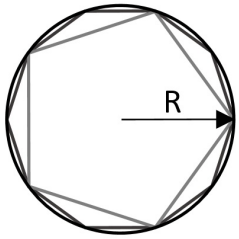

Figure 1.5.1: WGMs ray paths as inscribed regular polygons

From geometric optics, three empirical rules are set forth [76]. One, in a homogeneous medium light travels in straight lines. Two, the angle which light reflects from a surface equals the angle of incidence. Three, the path of light passing from one medium to another obeys Snell's law. Since light is confined in a resonator by total internal reflection, rules one and two give a description of the light path inside. Figure 1.5.1 shows how ray paths can be modeled as regular polygons that inscribe the resonator boundary. Smaller resonance wavelengths equate to higher order polygons. In the limit as the wavelength approaches zero, the resonator is much larger than the wavelength of light. Mathematically, $R \gg 1$ and the ray path polygon defines a circle tracing the resonator boundary. The path length travelled by photons inside the resonator equals the resonator's equatorial belt. To acheive resonance, the path of circulating light must overlap in phase. Applying the phase-matching principle of resonance gives [77, 78]

Geometric resonance condition

$$\frac{\lambda}{n_r} m = 2\pi R \tag{1.5.1}$$

where n_r is the refractive index of the resonator, λ is the resonance wavelength, and m is the azimuthal mode number. So for the mth and $(m+1)^{\text{th}}$ mode, the resonance conditions are

Geometric resonance condition for m^{th} mode

$$\frac{1}{\lambda_m} = \frac{m}{2\pi R n_r} \tag{1.5.2}$$

and

Geometric resonance condition for $(m+1)^{th}$ mode

$$\frac{1}{\lambda_{m+1}} = \frac{m+1}{2\pi R n_r} \tag{1.5.3}$$

Subtracting 1.5.2 from 1.5.3,

Deriving geometric free spectral range

$$\frac{\lambda_m - \lambda_{m+1}}{\lambda_m \lambda_{m+1}} = \frac{1}{2\pi R n_r} \tag{1.5.4}$$

This yields the free spectral range (FSR) depicted in Figure 1.5.2 and defined as the spacing between any two successive modes. Setting $m = 0$ in 1.5.4 gives

Geometric free spectral range

$$FSR = \lambda_0 - \lambda_1 = \frac{\lambda_0 \lambda_1}{2\pi R n_r} \cong \frac{\lambda_0^2}{2\pi R n_r} \tag{1.5.5}$$

where the approximation was made that $\lambda_0 \cong \lambda_1$. This result is reasonably accurate so long as the resonator circumference is much greater than the resonance wavelength. The extent of energy dissipation of a resonance is expressed by the quality factor Q, defined as [77, 78]

Definition of quality factor

$$Q = \frac{2\pi \text{Stored energy}}{\text{Energy lost per cycle}} = \frac{-\omega_0 U}{\frac{dU}{dt}} \tag{1.5.6}$$

where ω_0 is the resonance frequency in radians and U is the resonance's stored energy. The temporal solution to 1.5.6 for the stored energy is [77, 78]

Stored energy dissipation of resonance

$$U(t) = U_0 \exp(-\omega_0 t/Q) \tag{1.5.7}$$

The time dependence of the stored energy suggests the field amplitude dampens as

Field dissipation of resonance

$$E(t) = E_0 \exp(-\omega_0 t/2Q) \exp(i\omega_0 t) \tag{1.5.8}$$

Fourier analysis demonstrates that the energy distribution near resonance has the following proportion

Resonance Lorentzian lineshape

$$|E(\omega)|^2 \propto \frac{1}{(\omega - \omega_0)^2 + (\omega_0/2Q)^2} \tag{1.5.9}$$

The resonance lineshape is Lorentzian where the fullwidth half maximum ($FWHM$) is [77, 78]

Resonance linewidth

$$FWHM = \Delta\omega = \frac{\omega_0}{Q} \tag{1.5.10}$$

This provides another useful relation for Q [77, 78]

Resonance Q-factor

$$\begin{aligned} Q &= \frac{\text{Resonance position}}{FWHM} \\ &= \omega_0/\Delta\omega \\ &\cong \lambda_0/\Delta\lambda \end{aligned} \tag{1.5.11}$$

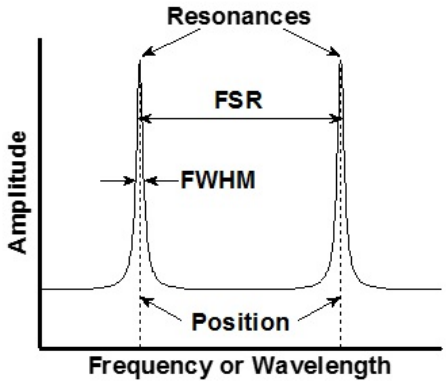

Figure 1.5.2: Resonance features identifiable from spectral measurements

1.6 Electromagnetic theory

1.6.1 Maxwell's equations

Maxwell's equations (MEs) give the appropriate description of macroscopic fields in free space. In SI units, MEs are

$$\nabla \times \mathbf{E}(\mathbf{r},t) = -\frac{\partial \mathbf{B}(\mathbf{r},t)}{\partial t} \tag{1.6.1}$$

$$\nabla \times \mathbf{H}(\mathbf{r},t) = \mathbf{J}_f(\mathbf{r},t) + \frac{\partial \mathbf{D}(\mathbf{r},t)}{\partial t} \tag{1.6.2}$$

$$\nabla \cdot \mathbf{D}(\mathbf{r},t) = \rho_f \tag{1.6.3}$$

$$\nabla \cdot \mathbf{B}(\mathbf{r},t) = 0 \tag{1.6.4}$$

Scalar and vector field quantities discussed in this section are real functions of space and time. $\mathbf{E}$ and $\mathbf{H}$ are corresponding electric and magnetic field intensity. $\mathbf{D}$ is the displacement current and $\mathbf{B}$ is the magnetic induction. Terms $\mathbf{J}_f$ and ρ_f denote the source densities of free currents and charge, respectively. Dielectric materials routinely encountered in optics may be considered to be source-free so that $\mathbf{J}_f$ and ρ_f are identically zero. The time-dependent, source-free MEs are:

$$\nabla \times \mathbf{E}(\mathbf{r}, t) = -\frac{\partial \mathbf{B}(\mathbf{r}, t)}{\partial t} \tag{1.6.5}$$

$$\nabla \times \mathbf{H}(\mathbf{r}, t) = \frac{\partial \mathbf{D}(\mathbf{r}, t)}{\partial t} \tag{1.6.6}$$

$$\nabla \cdot \mathbf{D}(\mathbf{r}, t) = 0 \tag{1.6.7}$$

$$\nabla \cdot \mathbf{B}(\mathbf{r}, t) = 0 \tag{1.6.8}$$

Fields $\mathbf{E}$ and $\mathbf{H}$ are independent. Fields $\mathbf{D}$ and $\mathbf{B}$ are related to $\mathbf{E}$ and $\mathbf{H}$ via constitutive equations whose form depends on the medium. These relations are cast using concepts of bound charges and currents that give rise respectively to the electric polarization $\mathbf{P}$ and magnetic polarization $\mathbf{M}$:

$$\mathbf{D} = \epsilon_0 \mathbf{E} + \mathbf{P} \tag{1.6.9}$$

$$\mathbf{B} = \mu_0 (\mathbf{H} + \mathbf{M}) \tag{1.6.10}$$

The electric and magnetic polarizations $\mathbf{P}$ and $\mathbf{M}$ represent the densities of induced electric and magnetic dipole moments in a medium. Constants ϵ_0 and μ_0 are the permittivity and permeability of free space. In materials with finite conductivity σ, for example metals, unbound charges put into motion by the

electric field $\mathbf{E}$ generate electric currents described by Ohm's Law, $\mathbf{J}_f = \sigma\mathbf{E}$. The charge and currents in typical dielectrics and metals are negligible under most circumstances. For a homogeneous, isotropic medium, the electric constitutive equation reads $\mathbf{P} = \epsilon_0\chi_e\mathbf{E}$, where χ_e is the electric susceptibility. The electric displacement becomes

$$\mathbf{D} = \epsilon_0(1 + \chi_e)\mathbf{E} = \epsilon_r\epsilon_0\mathbf{E} = \epsilon\mathbf{E} \tag{1.6.11}$$

so that the electric permittivity is $\epsilon_r = 1+\chi_e$. Similarly, the magnetic constitutive equation reads $\mathbf{M} = \mu_0\chi_m\mathbf{H}$, where χ_m is the magnetic susceptibility. The magnetic induction becomes

$$\mathbf{B} = \mu_0(1 + \chi_m)\mathbf{H} = \mu_r\mu_0\mathbf{H} = \mu\mathbf{H} \tag{1.6.12}$$

so that the magnetic permeability is $\mu_r = 1 + \chi_m$. Since the driving response of the electric and magnetic polarizations cannot be instantaneous, the expressions will generally be frequency dependent. These dependencies are accounted for by temporally dispersive definitions of the material parameters. The Lorentz force $d\mathbf{F}$ acting upon an infinitesimal volume element dV,

$$d\mathbf{F} = (\rho_f\mathbf{E} + \mathbf{J}_f \times \mathbf{B})dV \tag{1.6.13}$$

provides the final supplement. Together, the relationships outlined in this section provide a sufficient framework for most classical electromagnetic phenomena. However, boundary conditions must be made explicit in order to solve any electrodynamics problem of practical importance.

1.6.2 Boundary conditions

Electromagnetic fields are continuous in time and homogeneous media but are discontinuous at interfaces between physically different materials. MEs applied at physical boundaries give the necessary boundary conditions, which in general for time-dependent spatial fields are:

$$\mathbf{n}_{12} \times (\mathbf{E}_2 - \mathbf{E}_1) = 0 \tag{1.6.14}$$

$$\mathbf{n}_{12} \times (\mathbf{H}_2 - \mathbf{H}_1) = \mathbf{J}_s \tag{1.6.15}$$

$$\mathbf{n}_{12} \cdot (\mathbf{D}_2 - \mathbf{D}_1) = \rho_s \tag{1.6.16}$$

$$\mathbf{n}_{12} \cdot (\mathbf{B}_2 - \mathbf{B}_1) = 0 \tag{1.6.17}$$

where $\mathbf{n}_{12}$ is a normal unit vector at $\mathbf{r}$ on the interface between medium 1 and medium 2 and $\mathbf{J}_s$ and ρ_s are the free currents and charge density, respectively.

1.6.3 Phasor representation

Conciseness and convenience of manipulation have made phasor representation into a standard practice to describe fields that vary sinusoidally in time. The time-domain field vectors and corresponding frequency-domain phasors are related using Euler's formula. For instance,

$$\mathbf{E}(\mathbf{r}, t) = E_0 \cos(kz - \omega t) = \mathrm{Re}\{\mathbf{E}(\mathbf{r}, \omega) e^{-i\omega t}\} \tag{1.6.18}$$

Here, the time-harmonic convention $e^{-i\omega t}$ is used. The phasor represents a unit vector in the complex plane rotating clockwise with angular frequency ω. The $\mathrm{Re}\{\cdot\}$ operator performs the vector projection of the phasor onto the real axis

making the required association to the cosine function. The advantage this time-harmonic convention affords is a simplifying transformation $\frac{\partial}{\partial t} \Leftrightarrow -i\omega$ as one moves from the time-domain to the frequency-domain.

Thus, MEs can be recast using the phasor representation

$$\nabla \times \mathbf{E}(\mathbf{r}, \omega) = i\omega \mathbf{B}(\mathbf{r}, \omega) \tag{1.6.19}$$

$$\nabla \times \mathbf{H}(\mathbf{r}, \omega) = -i\omega \mathbf{D}(\mathbf{r}, \omega) \tag{1.6.20}$$

$$\nabla \cdot \mathbf{D}(\mathbf{r}, \omega) = 0 \tag{1.6.21}$$

$$\nabla \cdot \mathbf{B}(\mathbf{r}, \omega) = 0 \tag{1.6.22}$$

where $\mathbf{E}(\mathbf{r}, \omega)$, $\mathbf{H}(\mathbf{r}, \omega)$, and so forth are the phasor counterparts of $\mathbf{E}(\mathbf{r}, t)$, $\mathbf{H}(\mathbf{r}, t)$, and so forth and ω is the angular frequency. Most generally, $\mathbf{E}(\mathbf{r}, \omega)$, $\mathbf{H}(\mathbf{r}, \omega)$, $\mathbf{D}(\mathbf{r}, \omega)$, and $\mathbf{B}(\mathbf{r}, \omega)$ are complex functions of space and angular frequency. Similar conversions can be performed upon the constitutive relations and boundary conditions. The utility of doing this conversion will become apparent in ensuing discussions of the uniform plane wave and Poynting vector.

1.6.4 Uniform plane wave

In combination with phasor representation, a uniform plane wave proves to be a handy albeit fictitious description of a wave. A plane wave is defined as a wave for which the surfaces of constant phase are infinite planes, perpendicular to the direction of propagation. A uniform plane has the additional property that its wave amplitude is the same everywhere on any constant phase plane. Consider

a uniform plane wave propagating in free space in an arbitrary direction $\mathbf{k}$. The electric and magnetic field intensities can be written as

$$\mathbf{E} = \mathbf{E}_0 e^{-i\mathbf{k}\cdot\mathbf{r}} \tag{1.6.23}$$

$$\mathbf{H} = \mathbf{H}_0 e^{-i\mathbf{k}\cdot\mathbf{r}} \tag{1.6.24}$$

where $\mathbf{E}_0$ and $\mathbf{H}_0$ are the respective amplitudes of the electric and magnetic fields and $\mathbf{k}$ is the wavevector in free space. These field definitions can be substituted into the time-harmonic MEs to yield relations between various plane wave parameters

$$|\mathbf{k}| = k = \omega\sqrt{\mu_0\epsilon_0} \tag{1.6.25}$$

and

$$\mathbf{H}_0 = \sqrt{\frac{\epsilon_0}{\mu_0}}\hat{\mathbf{k}} \times \mathbf{E}_0 \tag{1.6.26}$$

In an isotropic medium, the wavevector $\mathbf{k}$ points in the direction of wave propagation. The magnitude of the wavevector is the wavenumber k alternatively defined as $k = 2\pi/\lambda$ where λ is the free space wavelength. For a plane wave, electric and magnetic field amplitudes are related to the wavevector by a vector cross product. Thus, constant phase planes are arranged perpendicular to the direction of propagation.

1.6.5 Evanescent wave

Light that experiences total internal reflection at a boundary between dielectric media can generate an evanescent wave. Evanescent waves are known to penetrate with decaying field amplitude from a higher index medium into a lower index medium. This characteristic property of evanescent waves is used as the basis of several high efficiency coupling devices. In the context of coupling light from an optical fiber to a sphere, the behavior and means of generating an evanescent wave is worth attention.

Consider the behavior of light that strikes a dielectric interface for a plane wave incident at an angle θ_1 to the dielectric interface (Figure 1.6.1) [79, 80]. The interface separates two semi-infinite media with refractive indices n_1 and n_2 where $n_1 > n_2$ such that medium 1 is the optically denser medium. For small θ_1 near normal incidence, the incident light wave will produce a reflected wave in medium 1 and a transmitted wave in medium 2. The reflected wave moves at an angle equal and opposite to the incident angle. Phase matching demands that the transmitted wave moves at an angle θ_2 given by Snell's law:

$$n_1 \sin\theta_1 = n_2 \sin\theta_2 \tag{1.6.27}$$

If the incident angle equals the critical angle, the transmitted wave moves parallel to the interface. Light incident at the critical angle is shown in Figure 1.6.1(c). Mathematically, $\theta_1 = \theta_c = \arcsin(n_2/n_1)$, so that $\theta_2 = 90^{\circ}$. For a glass-air interface, where $n_1 = 1.45$ and $n_2 = 1$, the critical angle is $\theta_c = 43.6^{\circ}$.

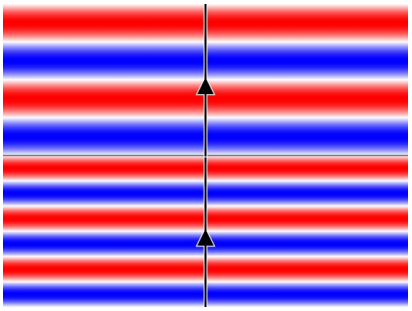

(a) Incidence normal to boundary ($\theta_1 = 90°$).

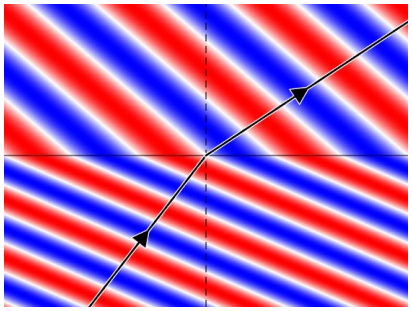

(b) Incidence below the critical angle ($\theta_1 < \theta_c$).

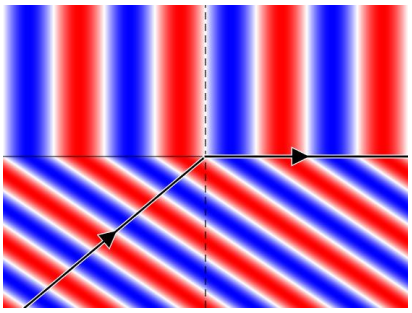

(c) Incidence at the critical angle ($\theta_1 = \theta_c$).

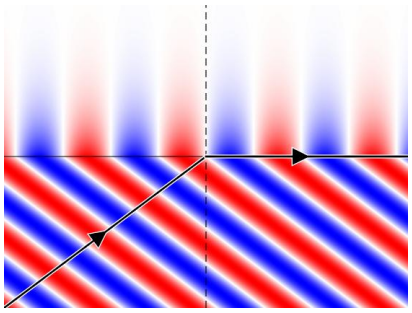

(d) Incidence beyond the critical angle ($\theta_1 > \theta_c$) showing total internal reflection.

Figure 1.6.1: Incident and transmitted plane waves for different incident angles between a higher index medium (bottom: n_1) and lower index medium (top: n_2)

There is no propagating transmitted wave if the incident angle exceeds the critical angle, *i.e.* $\theta_c < \theta_1 < 90^{\circ}$. This is the case of total internal reflection shown in Figure 1.6.1(d). For total internal reflection, no power crosses the interface, but an evanescent wave penetrates with decaying field amplitude into the low index medium. Despite having no real solution, an expression for the refraction angle θ_2 can be found by substitution Snell's law into the trigonometric identity $\sin^2\theta + \cos^2\theta = 1$ to give

$$\cos\theta_2 = \pm\sqrt{\left(\frac{n_1}{n_2}\right)^2 \sin^2\theta_1 - 1} \tag{1.6.28}$$

Light penetrating medium 2 would have an electric field given by

$$E(x,z) = T_0 \exp\left[-i\omega t + ik_2\left(x\sin\theta_2 + z\cos\theta_2\right)\right] \tag{1.6.29}$$

where $\omega = 2\pi\nu$ is an angular frequency. The wavenumber in medium 2 is $k_2 = 2\pi/\lambda_2$, where λ_2 is the wavelength in medium 2. Substitution of (1.6.28) into (1.6.29) gives [79, 80]

$$E(x,z) = T_0 \exp\left[-i\omega t + ik_2\left(\frac{n_1}{n_2}x\sin\theta_1 \pm iz\sqrt{\left(\frac{n_1}{n_2}\right)^2 \sin^2\theta_1 - 1}\right)\right] \tag{1.6.30}$$

To guarantee a finite electric field for large z, only the positive sign is kept. The final meaningful expression of the transmitted field is

$$E(x,z) = T_0 \exp\left(-i\omega t + ik_2\frac{n_1}{n_2}x\sin\theta_1\right)\exp\left(-k_2 z\sqrt{\left(\frac{n_1}{n_2}\right)^2 \sin^2\theta_1 - 1}\right) \tag{1.6.31}$$

This expression for the transmitted field describes an evanescent wave for which no energy is carried across the boundary. Showing exponential decay in the direction

normal to the boundary surface, it moves parallel to the interface with wavelength $\lambda_x = \lambda_1/\sin\theta_1$. The result indicates that the field decays exponentially with increasing z, so that the field amplitude reduces by $1/e$ of its value at the boundary at the distance of one decay length. By this definition, the decay length is [79, 80]

$$\Lambda = \frac{1}{k_2\sqrt{\left(\frac{n_1}{n_2}\right)^2 \sin^2\theta_1 - 1}} \tag{1.6.32}$$

$$= \frac{\lambda_2}{2\pi\sqrt{\left(\frac{n_1}{n_2}\right)^2 \sin^2\theta_1 - 1}} \tag{1.6.33}$$

which shows the penetration depth into medium 2 is on the same order as λ_2.

1.6.6 Poynting vector

The conservation of energy for electromagnetic fields is captured by Poynting's theorem. The theorem introduces the Poynting vector $\mathbf{S}$ in W/m^2, which represents the radiant energy flux density by a magnitude and direction. The quantity is experimentally important because it constitutes measurable powers associated with electromagnetic fields. In free space, the Poynting theorem reads $\nabla \cdot \mathbf{S} + \partial u/\partial t = 0$, where $\mathbf{S} = \mathbf{E} \times \mathbf{H}$ is the Poynting vector and $u = (\mathbf{E} \cdot \mathbf{D} + \mathbf{H} \cdot \mathbf{B})/2$ is the electromagnetic energy density. Phasor representation assists the description for the time-averaged Poynting vector $\langle \mathbf{S} \rangle$ so that

$$\langle \mathbf{S} \rangle = \frac{1}{2}\mathrm{Re}\left\{\mathbf{E} \times \mathbf{H}^*\right\} \tag{1.6.34}$$

Chapter 2

Mie theory

2.1 Introduction

This chapter covers the interaction between radiation and matter that is specifically relevant for light incident on a spherical particle. Matter is made up of discrete electric charges such as electrons and protons. Light that strikes a particle causes these charges to oscillate and culminates in the emission of secondary radiation called scattering. In an absorbing particle whose index of refraction is complex-valued, some light goes unscattered and is extinguished within the particle. After its encounter with the particle, the incident light is effectively weakened by scattering and absorption. The net reduction of radiation from the incident beam is called extinction.

The two primary ways used to treat the interaction of light with a particle are: (1) geometric optics and (2) Mie theory. Geometric optics provides a model

based not on light waves, but rather upon light rays. The model assumes that the wavelength is much smaller than any relevant physical dimension. This corresponds to large size parameters which in practice translates roughly to $R > 20\lambda$. Though its validity is restricted, the formulation of geometric optics provides a simple scheme for particle-light interaction. Free from vectors or infinite series in its results, several fundamental relations can be derived with minimum effort as shown in section 1.5. Mie theory was developed by Gustav Mie in 1908 to explain the color of gold colloids [81]. The theory is conceptualized using electromagnetic waves and applies Maxwell's equations to derive incident, scattered, and internal fields of a particle. Field expressions arise as infinite series expansions of vector spherical harmonics (VSWFs) from which further calculations yield cross sections, efficiency factors, and if desired even intensity distributions in the particle. These parameters can be studied under different circumstances to reveal the nature of effects such as the incidence angle of light, particle geometry, and the relative refractive index of the particle to its surrounding environment. Mie theory also reveals the behavior of morphology-dependent resonances (MDRs) which have special importance. MDRs may be charted versus the size parameter defined by [77]

$$x = \frac{2\pi n_M R}{\lambda} \tag{2.1.1}$$

where R denotes the particle radius and λ/n_M represents the wavelength in the surrounding medium with index n_M. The vector formulation and infinite series

lend complexity to Mie theory, but its detail and completeness make it the most reliable model for particle-light interaction.

The following sections present a complete analysis of Mie theory for the general case of plane wave excitation. The case assumes an incident plane wave, $\hat{\mathbf{x}}-$polarized with amplitude E_0, traveling along the $\hat{\mathbf{z}}$ direction, given by

$$\mathbf{E}_{inc} = E_0 e^{i\beta_0 z}\hat{\mathbf{x}} \tag{2.1.2}$$

The wave equation is developed from Maxwell's equations. Scalar and vector solutions are sought to form the subsequent field expressions. Separation into radial and angular dependencies happens here. The importance of recurrence relations to the description of fields is shown for a sphere in the Mie regime. Next, the incident, scattered, and transmitted fields are provided. Lastly, cross sections are considered after applied boundary conditions for Mie scattering internal coefficients derived before.

Having outlined the fundamentals of Mie theory, the investigation continues with the cross sections of a simple, lossless dielectric sphere. Effects of particle size, absorption, and index of the surrounding medium are considered. Mie theory is then extended to study the case of interaction between an evanescent wave and spherical particle. An exploration is made of the dependence on incident angle demonstrated by an evanescent wave versus a plane wave. Insight into the enhanced excitation of MDRs will prove instructional in later chapters that detail the design of optical fiber structures that support WGMs.

2.2 Maxwell's equations

From Maxwell's equations,

$$\nabla \times \mathbf{E} = i\omega\mu\mathbf{H} \tag{2.2.1}$$

$$\nabla \times \mathbf{H} = -i\omega\epsilon\mathbf{E} \tag{2.2.2}$$

Taking the curl of (2.2.1) and (2.2.2) gives

$$\nabla \times \nabla \times \mathbf{E} = i\omega\mu\nabla \times \mathbf{H} = \omega^2\epsilon\mu\mathbf{H} \tag{2.2.3}$$

$$\nabla \times \nabla \times \mathbf{H} = -i\omega\epsilon\nabla \times \mathbf{E} = \omega^2\epsilon\mu\mathbf{E} \tag{2.2.4}$$

Applying the vector identity

$$\nabla \times \nabla \times \mathbf{A} = \nabla(\nabla \cdot \mathbf{A}) - \nabla \cdot (\nabla\mathbf{A}) \tag{2.2.5}$$

to (2.2.3) and (2.2.4) yields time-dependent vector wave equations

$$\nabla^2\mathbf{E} + k^2\mathbf{E} = 0 \tag{2.2.6}$$

$$\nabla^2\mathbf{H} + k^2\mathbf{H} = 0 \tag{2.2.7}$$

where $k^2 = \omega^2\epsilon\mu$ denotes a wave vector, ϵ is electric permittivity, and μ is magnetic permeability.

The goal now is to derive the vector solutions of the wave equation. The strategy will be to section the problem space into homogeneous regions, namely the regions inside and outside spherical particle. The wave equations (2.2.6) and (2.2.7) will be solved generically for each region. Applying appropriate boundary conditions will then uniquely identify the final solution. For convenience, the following considerations are heeded [82]

1. Choose a spherical coordinate system (r, θ, ϕ) to match problem symmetry
2. Define a scalar function ψ_{lm}
3. Define a constant vector $\mathbf{r}$

Let the scalar function be a solution of

$$\nabla^2 \psi_{lm} + k^2 \psi_{lm} \tag{2.2.8}$$

This form of scalar function can be described by three independent vector solutions given as [82, 83]

$$\mathbf{L} = \nabla \psi_{lm} \tag{2.2.9}$$

$$\mathbf{M}_{lm} = \nabla \times \mathbf{r} \psi_{lm} \tag{2.2.10}$$

$$\mathbf{N}_{lm} = \frac{1}{k} \nabla \times \mathbf{M}_{lm} \tag{2.2.11}$$

By inspection, the wave equations (2.2.6) and (2.2.8) are satisfied by vector solutions $\mathbf{L}$, $\mathbf{M}_{lm}$, and $\mathbf{N}_{lm}$. Solenoidal functions $\mathbf{M}_{lm}$ and $\mathbf{N}_{lm}$ related by the curl operator are transverse waves analogous to $\mathbf{E}$ and $\mathbf{H}$, but the irrotational function $\mathbf{L}$ represents a longitudinal wave and is therefore dropped from this analysis [82].

2.3 Scalar solution

In spherical coordinates, the scalar solution ψ_{lm} in (2.2.8) is a function of (r, θ, ϕ) which can be expressed by [82, 83, 84, 85]

$$\frac{1}{r^2} \frac{\partial}{\partial r} \left(r^2 \frac{\partial \psi}{\partial r} \right) + \frac{1}{r^2 \sin\theta} \frac{\partial}{\partial \theta} \left(\sin\theta \frac{\partial \psi}{\partial \theta} \right) + \frac{1}{r^2 \sin^2\theta} \frac{\partial^2 \psi}{\partial \phi^2} + k^2 \psi = 0 \tag{2.3.1}$$

A product solution is sought in the form of

$$\psi(r, \theta, \phi) = R(r) \Theta(\theta) \Phi(\phi) \tag{2.3.2}$$

The main advantage of separation of variables is the transformation of a single multivariable partial differential equation into three univariable ordinary differential equations. Defining m and L as separation constants, the three components and their solutions are [82, 83, 84, 85]

Azimuthal

$$\frac{d^2\Phi}{d\phi^2} + m^2\Phi = 0 \tag{2.3.3}$$

$$\Phi = e^{\pm im\phi} \tag{2.3.4}$$

Polar

$$(1-\cos^2\theta)\frac{d^2\Theta}{d(\cos\theta)^2} - 2\cos\theta\frac{d\Theta}{d(cos\theta)} + \left[L - \frac{p^2}{(1-\cos^2\theta)}\right] = 0 \tag{2.3.5}$$

By substituting $L = l(l+1)$, (2.3.5) resembles an associated Legendre equation such that [82, 83, 84, 85]

$$\begin{aligned}\Theta &= P_l^m(\eta) \\ &= \frac{(1-\eta^2)^{\frac{m}{2}}}{2^l l!}\frac{d^{l+m}(\eta^2-1)^l}{d(\eta)^{l+m}}\end{aligned} \tag{2.3.6}$$

where $\eta = \cos\theta$ is used.

Radial

$$r^2\frac{d^2R}{dr^2} + 2r\frac{dR}{dr} + (k^2r^2 - L^2)R = 0 \tag{2.3.7}$$

The solution of (2.3.7) is [82, 83, 84, 85]

$$R = \sqrt{\frac{2}{\pi}}z_l(\rho) \tag{2.3.8}$$

where $\rho = kr$ and $z_l(\rho)$ is either the spherical Bessel function $j_l(\rho)$ or spherical Hankel function of the first kind $h_l(\rho)$. The choice of these radial functions is motivated by where they exhibit finite values. Since $j_l(\rho)$ is finite at the origin, it accurately describes both the incident and transmitted fields. Conversely, $h_l(\rho)$ is finite in the far field and behaves as an outgoing spherical wave which accurately describes the scattered field.

Separate solutions for R, Θ, and Φ from (2.3.8), (2.3.6), and (2.3.4) combine to form the product solution presumed in (2.3.2).

$$\psi_{lm}(r,\theta,\phi) = \sqrt{\frac{2}{\pi}} z_l(kr) P_l^m(\cos\theta) e^{\pm im\phi} \tag{2.3.9}$$

In consideration that the azimuthal component $e^{\pm im\phi}$of (2.3.9) is proportional to $\cos(m\phi)$ and $\sin(m\phi)$, even and odd functions, it is useful to recast the expression as

$$\psi_{\substack{e\\o}lm}(r,\theta,\phi) = \sqrt{\frac{2}{\pi}} z_l(kr) P_l^m(\cos\theta) \begin{matrix}\cos(m\phi)\\ \sin(m\phi)\end{matrix} \tag{2.3.10}$$

The subscripts e for even and o for odd account for the symmetry of the functions when the azimuthal angle changes from ϕ to $-\phi$. The scalar solution to ψ is concluded with (2.3.10) which will be used in the expansion of the vector solutions when deriving the electric and magnetic fields.

2.4 Vector solution

2.4.1 Vector spherical harmonics $\mathbf{M}_{lm}$ and $\mathbf{N}_{lm}$

The vector $\mathbf{M}_{lm}$ originally defined in (2.2.10) is now recast using the scalar expression from (2.3.10)

$$\mathbf{M}_{\substack{e\\o}lm} = \nabla \times \hat{\mathbf{r}} \left(r\psi_{\substack{e\\o}lm} \right) \tag{2.4.1}$$

where the relation $\mathbf{r} = \hat{\mathbf{r}}r$ has been used. To find $\mathbf{M}_{lm}$, the operation in (2.4.4) is done for even and odd modes which are organized into separate matrices as follows

$$\mathbf{M}_{elm} = \begin{pmatrix} 0 \\ -\sin(m\phi)\dfrac{mP_{lm}(\eta)}{\sin\theta} z_l(\rho) \\ -\cos(m\phi)\dfrac{dP_{lm}(\eta)}{d\theta} z_l(\rho) \end{pmatrix} \tag{2.4.2}$$

$$\mathbf{M}_{olm} = \begin{pmatrix} 0 \\ -\cos(m\phi)\dfrac{mP_{lm}(\eta)}{\sin\theta} z_l(\rho) \\ -\sin(m\phi)\dfrac{dP_{lm}(\eta)}{d\theta} z_l(\rho) \end{pmatrix} \tag{2.4.3}$$

where $\eta = \cos\theta$ and $\rho = kr$ have been used [82, 83, 77, 86].

The vector $\mathbf{N}_{lm}$ originally defined in (2.2.11) is also recast using the updated expression in (2.4.1).

$$\mathbf{N}_{\substack{e\\o}lm} = \frac{1}{k}\nabla \times \mathbf{M}_{\substack{e\\o}lm} \tag{2.4.4}$$

To find $\mathbf{N}_{lm}$, the operation in (2.4.4) is done upon (2.4.2) and (2.4.3) for even and odd modes which are organized into separate matrices as follows

$$\mathbf{N}_{elm} = \begin{pmatrix} \cos(m\phi) l(l+1) P_{lm}(\eta) \dfrac{z_l(\rho)}{d\rho} \\ \cos(m\phi) \dfrac{m P_{lm}(\eta)}{\sin\theta} \dfrac{1}{\rho} \dfrac{d}{d\rho}[\rho z_l(\rho)] \\ -\sin(m\phi) \dfrac{dP_{lm}(\eta)}{d\theta} \dfrac{1}{\rho} \dfrac{d}{d\rho}[\rho z_l(\rho)] \end{pmatrix} \tag{2.4.5}$$

$$\mathbf{N}_{olm} = \begin{pmatrix} \sin(m\phi) l(l+1) P_{lm}(\eta) \dfrac{z_l(\rho)}{d\rho} \\ \sin(m\phi) \dfrac{dP_{lm}(\eta)}{d\theta} \dfrac{1}{\rho} \dfrac{d}{d\rho}[\rho z_l(\rho)] \\ -\sin(m\phi) \dfrac{m P_{lm}(\eta)}{\sin\theta} \dfrac{1}{\rho} \dfrac{d}{d\rho}[\rho z_l(\rho)] \end{pmatrix} \tag{2.4.6}$$

where $\eta = \cos\theta$ and $\rho = kr$ have again been used [82, 83, 77, 86].

Any arbitrary solution for the electromagnetic fields can be expanded as an infinite series of these functions. The most useful solution in this context is the sum of two special and independent modes: transverse electric (TE) and transverse magnetic (TM). Transverse modes are electromagnetic fields defined to have zero longitudinal component. In spherical coordinates, TE modes are absent an electric radial component ($E_r = 0$) and TM modes are absent a magnetic radial component ($H_r = 0$). Having chosen the reference frame with the $\hat{\mathbf{z}}$-axis coincident with the propagation of the incident plane wave, symmetry of a sphere sets the simple constraint $m = \pm 1$ [82]. Later, we consider an extension to Mie theory for an incident evanescent wave for which this symmetry is broken [86].

2.5 Electromagnetic fields for a sphere

Using spherical harmonics, we express the electromagnetic fields of waves incident upon, scattered from, and interior to a spherical particle. The sphere is assumed to be embedded in a lossless medium with real-valued refractive index n_M.The refractive index of the particle n_s may be complex-valued to account for absorption in the sphere. Illuminating the sphere is an incident plane wave with wavenumber $k_M = 2\pi n_M/\lambda$ where λ is the wavelength. The relative refractive index is given by $N = n_s/n_M$. The size parameter is defined as $x = k_M R$, so that $Nx = k_s R$.

Then, the electromagnetic fields for an $\hat{\mathbf{x}}$-polarized plane wave propagating along the $\hat{\mathbf{z}}$-axis, are as follows [82, 83, 77, 86]:

Incident wave:

$$\mathbf{E}_{inc} = E_0 \sum_{l=1}^{\infty} \frac{i^l(2l+1)}{l(l+1)} [\mathbf{M}_{ol1}^{(1)}(k_M) - i\mathbf{N}_{el1}^{(1)}(k_M)] \tag{2.5.1}$$

$$\mathbf{H}_{inc} = \frac{-k_M E_0}{\omega\mu_0} \sum_{l=1}^{\infty} \frac{i^l(2l+1)}{l(l+1)} [\mathbf{M}_{el1}^{(1)}(k_M) + i\mathbf{N}_{ol1}^{(1)}(k_M)] \tag{2.5.2}$$

Scattered wave:

$$\mathbf{E}_{sca} = -E_0 \sum_{l=1}^{\infty} \frac{i^l(2l+1)}{l(l+1)} [b_l \mathbf{M}_{ol1}^{(1)}(k_M) - ia_l \mathbf{N}_{el1}^{(1)}(k_M)] \tag{2.5.3}$$

$$\mathbf{H}_{sca} = \frac{k_M E_0}{\omega\mu_0} \sum_{l=1}^{\infty} \frac{i^l(2l+1)}{l(l+1)} [a_l \mathbf{M}_{el1}^{(1)}(k_M) + ib_l \mathbf{N}_{ol1}^{(1)}(k_M)] \tag{2.5.4}$$

Internal wave:

$$\mathbf{E}_{int} = E_0 \sum_{l=1}^{\infty} \frac{i^l(2l+1)}{l(l+1)} [\beta_l^1 \mathbf{M}_{ol1}^{(3)}(k_1) - i\alpha_l^1 \mathbf{N}_{el1}^{(3)}(k_1)] \tag{2.5.5}$$

$$\mathbf{H}_{int} = \frac{-k_1 E_0}{\omega \mu_0} \sum_{l=1}^{\infty} \frac{i^l(2l+1)}{l(l+1)} [\alpha_l^1 \mathbf{M}_{el1}^{(3)}(k_1) + i\beta_l^1 \mathbf{N}_{ol1}^{(3)}(k_1)] \tag{2.5.6}$$

The terms a_l and b_l are the respective expansion coefficients for TM and TE modes of the scattered wave. Likewise, terms α_l^1 and β_l^1 are the respective expansion coefficients for TM and TE modes of the wave inside the particle. Note the change in sign of field expressions for the incident and internal waves versus the scattered wave. Also, the wavenumber dependence is k_1 for the wave inside the particle but k_M outside for incident and scattered waves. With a reference frame centered on the spherical particle, spherical Bessel functions for the field expansions inside and outside the sphere are chosen to ensure field singularity at the origin and at remote distances.

Spherical Bessel functions j_l (superscript 1 of the vector harmonics) are used in the expansions of the electromagnetic fields for the wave incident and inside the particle. Spherical Hankel functions $h_l^{(1)}$ (superscript 3 of the vector harmonics) are used in the expansion of the scattered wave to represent outgoing spherical waves. This representation is predicated by the time-harmonic ansatz $e^{-i\omega t}$ for which a complex refractive index is defined. Else, assuming $e^{+i\omega t}$, $h_l^{(2)}$ rather than $h_l^{(1)}$ would represent an outgoing spherical wave.

The field construction presents as a sum over l because the fields are expanded

into linear independent radiating multipoles of order l. The sum starts at order $l = 1$ representing a radiating dipole and continues over l to infinity. In practice, empirically observed cutoffs are used to terminate numerical summations.

2.6 Boundary conditions

Electromagnetic fields in regions of constant, isotropic permittivity and permeability are required to satisfy Maxwell's equations. However, boundaries between distinct regions demonstrate abrupt changes in these properties. The transition region for these changes has thickness of the order of atomic dimensions. At such boundaries, the continuity of tangential field components must be preserved.

$$[\mathbf{E}_{inc} + \mathbf{E}_{sca}] \times \hat{\mathbf{r}}|_{r=R} = \mathbf{E}_1 \times \hat{\mathbf{r}}|_{r=R} \tag{2.6.1}$$

By applying Maxwell's boundary conditions at the surface of the sphere at $r = R$, expansion coefficients a_l, b_l of the scattered wave and α_l^1, β_l^1 inside the sphere are uniquely determined. Resolving components and using orthogonality relations of associated Legendre polynomials yield the following equations [82, 84, 83, 86, 87]:

$$\alpha_l^1 \psi_n'(Nx) = N[\psi_l'(x) - a_l \xi_l'(x)] \tag{2.6.2}$$

$$\beta_l^1 \psi_n'(Nx) = \psi_l'(x) - b_l \xi_l'(x) \tag{2.6.3}$$

$$\alpha_l^1 \psi(Nx) = \psi_l'(x) - a_l \xi_l'(x) \tag{2.6.4}$$

$$\beta_l^1 \psi(Nx) = N[\psi_l(x) - b_l \xi_l(x)] \tag{2.6.5}$$

Abbreviations $\psi_l(y) = y j_l(y)$ and $\xi_l(y) = y h_l^{(1)}(y)$ are Ricatti-Bessel and Riccati-

Hankel functions respectively.

2.7 Expansion coefficients

The expansion coefficients are found from the system of equations resolved from Maxwell's boundary conditions [82, 83, 86, 87]. Values for each order l are found separately.

$$a_l = \frac{\psi_l(x)\psi_l'(Nx) - N\psi_l'(x)\psi_l(Nx)}{\xi_l(x)\psi_l'(Nx) - N\psi_l(Nx)\xi_l'(x)} \tag{2.7.1}$$

$$b_l = \frac{\psi_l(Nx)\psi_l'(x) - N\psi_l'(Nx)\psi_l(x)}{\xi_l'(x)\psi_l(Nx) - N\psi_l'(Nx)\xi_l(x)} \tag{2.7.2}$$

$$\alpha_l^1 = \frac{-iN}{\xi_l(x)\psi_l'(Nx) - N\psi_l(Nx)\xi_l'(x)} \tag{2.7.3}$$

$$\beta_l^1 = \frac{iN}{\xi_l'(x)\psi_l(Nx) - N\psi_l'(Nx)\xi_l(x)} \tag{2.7.4}$$

Note that corresponding coefficients a_l, α_l^1 and b_l, β_l^1 have identical denominators. As their denominators vanish, the expressions diverge. Consequently, the fields described by infinite series of the coefficients exhibit resonance peaks. These peaks occur according to conditions set by the physical properties of the particle. For this reason, the resonances are sometimes called structural or morphology-dependent resonances (MDRs). Specific factors that affect the coefficients and subsequent resonances are the incident wavelength, sphere size, and refractive indices of the sphere and surrounding medium. Details of the behavior of these resonances will be examined further in later sections for a lossless and lossy sphere.

2.8 Cross-sections and efficiencies

2.8.1 Scattering and extinction

Experimentally, the rates at which incident light is scattered and absorbed are more important than the fields themselves. The rates can be found by balancing the energy flux entering and leaving the sphere. The complex Poynting theorem is applied as a surface integration of the Poynting vector outside the particle to give the net rate of change in energy. Scattered and extinction cross sections in m^2 are then obtained using the relations [82, 83, 86, 87]:

$$\sigma_{sca} = \frac{W_{sca}}{I_{inc}} \tag{2.8.1}$$

$$\sigma_{ext} = \frac{W_{ext}}{I_{inc}} \tag{2.8.2}$$

where I_{inc} represents the intensity incident on the sphere surface. Scattered and extinction energies, W_{sca} and W_{ext} respectively, are given by

$$\begin{aligned} W_{sca} &= \frac{1}{2}\mathrm{Re}\int_0^{2\pi}\int_0^{\pi}\left(\mathbf{E}_{sca}\times\mathbf{H}^*_{sca}\right)R^2\sin\theta d\theta d\phi \\ &= \frac{1}{2}\mathrm{Re}\int_0^{2\pi}\int_0^{\pi}\left(E_{sca,\theta}H^*_{sca,\phi}-E_{sca,\phi}H^*_{sca,\theta}\right)R^2\sin\theta d\theta d\phi \end{aligned} \tag{2.8.3}$$

$$W_{ext} = \frac{1}{2}\mathrm{Re}\int_0^{2\pi}\int_0^{\pi}\left(\mathbf{E}_{inc}\times\mathbf{H}^*_{sca}+\mathbf{E}_{sca}\times\mathbf{H}^*_{inc}\right)R^2\sin\theta d\theta d\phi$$
$$= \frac{1}{2}\mathrm{Re}\int_0^{2\pi}\int_0^{\pi}\Big(E_{inc,\phi}H^*_{sca,\theta}-E_{inc,\theta}H^*_{sca,\phi}$$
$$-E_{sca,\theta}H^*_{inc,\phi}+E_{sca,\phi}H^*_{inc,\theta}\Big)R^2\sin\theta d\theta d\phi \qquad (2.8.4)$$

The absorbed energy is related to the scattered and extinction energies by $W_{abs} = W_{ext} - W_{sca}$. Respective substitution of (2.8.3) and (2.8.4) into (2.8.1) and (2.8.2) gives series representations for the corresponding scattered and extinction cross-sections.

$$\sigma_{sca} = \frac{2\pi}{k_m^2}\sum_{l=1}^{\infty}(2l+1)\left(a_l|H_{l,m}|^2+b_l|F_{l,m}|^2\right) \qquad (2.8.5)$$

$$\sigma_{ext} = \frac{2\pi}{k_m^2}\mathrm{Re}\sum_{l=1}^{\infty}(2l+1)\left(a_l|H_{l,m}|^2+b_l|F_{l,m}|^2\right) \qquad (2.8.6)$$

Angular functions $F_{l,m}$ and $H_{l,m}$ are related to $\Pi_{l,m}$ and $\tau_{l,m}$ by

$$F_{l,m} = \frac{2}{l(l+1)}\sum_{m=-l}^{l}\frac{(l-m)!}{(l+m)!}|\Pi_{l,m}|^2 \qquad (2.8.7)$$

$$H_{l,m} = \frac{2}{l(l+1)}\sum_{m=-l}^{l}\frac{(l-m)!}{(l+m)!}|\tau_{l,m}|^2 \qquad (2.8.8)$$

For plane wave excitation, all terms vanish besides $m = 1$ so that (2.8.5) and (2.8.6) reduce to

$$\sigma_{sca} = \frac{2\pi}{k_M^2}\sum_{l=1}^{\infty}(2l+1)\left(|a_l|^2+|b_l|^2\right) \qquad (2.8.9)$$

$$\sigma_{ext} = \frac{2\pi}{k_M^2}\mathrm{Re}\sum_{l=1}^{\infty}(2l+1)\left(a_l+b_l\right) \qquad (2.8.10)$$

However, such remarkable simplification is possible only for plane waves. If light were incident as an evanescent wave where $\theta_k > 0$, then multiple angular terms would contribute to the final cross-sections which may excite more resonant modes.

Dimensionless efficiency factors can be formed by normalizing versus the geometrical cross-section σ_{geo} given as πR^2 for a sphere of radius R. The extinction and scattering efficiencies respectively are

$$Q_{sca} = \frac{\sigma_{sca}}{\sigma_{geo}} \tag{2.8.11}$$

$$Q_{ext} = \frac{\sigma_{ext}}{\sigma_{geo}} \tag{2.8.12}$$

Explicit series solutions of the efficiency factors for scattering and extinction are

$$Q_{sca} = \frac{2}{x^2} \sum_{l=1}^{\infty} (2l+1) \left(|a_l|^2 + |b_l|^2 \right) \tag{2.8.13}$$

$$Q_{ext} = \frac{2}{x^2} \mathrm{Re} \sum_{l=1}^{\infty} (2l+1) (a_l + b_l) \tag{2.8.14}$$

using the size parameter defined earlier as $x = k_M R = 2\pi n_M R/\lambda$.

Figure 2.8.1 gives a plot of scattering efficiency versus size parameter. To mention some of the well-known features [45][46]–[50], the scattering efficiency shows a steep initial rise as the size parameter moves away from the Rayleigh limit ($x \ll 1$). For large size parameter, Q_{sca} approaches a steady-state value of two predicted by geometric optics theory. Lastly, it demonstrates rapid oscillations superposing a slowly changing background.

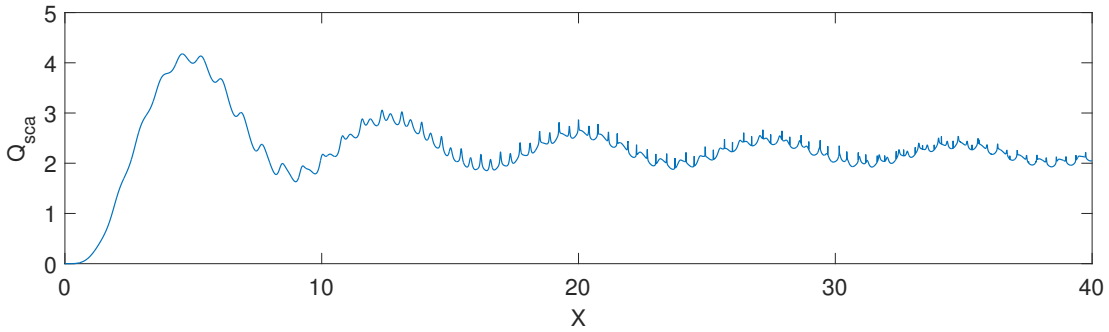

Figure 2.8.1: Scattering efficiency of a sphere with $n_s = 1.9$ in water

2.8.2 Near-field

Typical experiments measure absorption and scattering in the far-field at remote distances from the surface of a spherical particle. The scattering and extinction efficiencies, Q_{sca} and Q_{ext}, are sufficient in such circumstances to quantify the ability of a particle to scatter or extinguish incoming light at the incident wavelength. For information regarding the strength of the electromagnetic fields nearby the particle, different parameters are needed. Filling this requirement are the near-field efficiencies, Q_{nf} and Q_r, introduced in 1981 by Messinger *et al.* [88].

$$Q_{nf}(r) = \frac{r^2}{\pi R^2 I_0} \int_0^{2\pi} \int_0^{\pi} \mathbf{E}_{sca}(r) \cdot \mathbf{E}^*_{sca}(r) \sin\theta d\theta d\phi \tag{2.8.15}$$

$$Q_r(r) = \int_0^{2\pi} \int_0^{\pi} \mathbf{E}_{r,sca}(r) \cdot \mathbf{E}^*_{r,sca}(r) \sin\theta d\theta d\phi \tag{2.8.16}$$

In explanation, the near-field efficiency Q_{nf} is the square of the spatially averaged electric field of the scattered wave. However, the radial near-field efficiency Q_r is the square of just the radial component E_r of the electric field of the scattered

wave included as part of Q_{nf}. The radial component of the scattered electric field is a characteristic aspect of the near-field because it drops away in the far-field as r^{-1}. From (2.8.15) and (2.8.16), explicit relations for Q_{nf} and Q_r are [88]

$$Q_{nf}(r) = \left\{ \frac{2r^2}{R^2} \sum_{l=1}^{\infty} |a_l|^2 \left[(l+1) \left| h_{l-1}^{(1)} (k_M r) \right|^2 \right] + l \left| h_{l+1}^{(1)} (k_M r) \right|^2 \right. \tag{2.8.17}$$

$$\left. + (2l+1) |b_l|^2 \left| h_l^{(1)} (k_M r) \right|^2 \right\}$$

$$Q_r(r) = \frac{2}{(k_M R)^2} \sum_{l=1}^{\infty} (2l+1)(l+1) l |a_n|^2 \left| h_l^{(1)} (k_M r) \right|^2 \tag{2.8.18}$$

where $h_l^{(1)}$ is the Hankel function of the first kind ($e^{-i\omega t}$ time dependence assumed). Physically, the efficiency factor Q_{nf} measures the ability of a sphere to convert incident electric field intensity into near-field intensity. In the limit $r \gg R$, Q_{nf} decreases in approach of its asymptotic value Q_{sca}. Remarking upon Q_r, this efficiency factor measures the ability of sphere to convert incident electric field intensity into radially directed near-field intensity. The near-field efficiencies have been defined as functions of radius r from the sphere center, but particular convenience is afforded by evaluating them at the surface of the sphere at $r = R$. The near-field efficiencies at the spherical boundary become [88]

$$Q_{nf}|_{r=R} = 2\sum_{l=1}^{\infty}\left\{|a_l|^2\left[(l+1)\left|h_{l-1}^{(1)}(k_M R)\right|^2 + l\left|h_{l+1}^{(1)}(k_M R)\right|^2\right]\right. \tag{2.8.19}$$

$$\left. + (2l+1)|b_l|^2\left|h_l^{(1)}(k_M R)\right|^2\right\}$$

$$Q_r|_{r=R} = \frac{2}{(k_M R)^2}\sum_{l=1}^{\infty}(2l+1)(l+1)\,l\,|a_n|^2\left|h_l^{(1)}(k_M R)\right|^2 \tag{2.8.20}$$

As alluded to earlier, Q_{nf} comprises fields that increase faster than r^{-1} in approach from the far-field to the surface of the sphere. Consequently, Q_{nf} can be larger than Q_{sca} because it accounts for additional field components that occur only in the near-field. Figure 2.8.2 offers a plot of the near field efficiency versus size parameter. Field enhancement in the near field is so dramatic that the base-10 logarithm of its value must be presented. Clearly, coupling applications would benefit from utilizing near-field energy exchange because of the large resonances that are achievable in this region. These features are the same observed for the spectrum of Q_{sca} only magnified due to the rich composition of the near field.

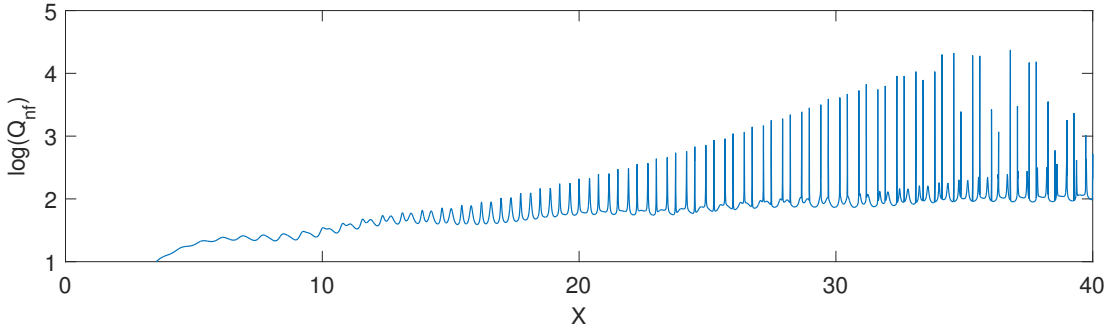

Figure 2.8.2: Base-10 logarithm of the near field scattering efficiency of a sphere with $n_s = 1.9$ in water

2.9 Resonances

This section seeks to uncover the behavior of WGM resonances hidden within the series solutions provided by Mie theory. Dependencies of the efficiency factors are explored and observed versus the dimensionless size parameter $x = 2\pi n_M R/\lambda$. In anticipation of later experiments discussed in chapter 4, the refractive index is chosen as $n_s = 1.9$ for a barium titanate sphere (BTO). Other assumptions, are made explicit as necessary for the discussion of different dependencies.

2.9.1 Multipole series expansion

The surrounding medium is first taken as water with refractive index $n_M = 1.33$. Also initially presumed is a lossless microsphere with zero imaginary part for its index where $\kappa = \mathrm{Im}\,(n_s) = 0$. Without absorption by the sphere, extinction is exclusively from scattering. In other words, for this case Q_{sca} and Q_{ext} are equal. Using (2.8.13) and summing l over 50 poles, Figure 2.9.1 depicts the total sum as well as the individual contribution of poles $l = 31, 32, 33$, and

34. Resonant enhancement due the individual poles demonstrates peaks that stick out prominently above slower variations. The size parameter x is inversely proportional to the incident wavelength, but is proportional to resonator size (radius) and the refractive index of the host medium. Again, the host medium is water so its index is fixed, that leaves two unspecified variables and thus two possible interpretations for the spectrum. In the first case, assuming a fixed wavelength, the plot indicates the resonances that occur for spheres of increasing size. In the second case, choosing a specific sphere size, the plot then indicates the resonances that may be observed for different incident wavelengths. This range of size parameter was chosen to clearly relate how individual poles can contribute strong resonances to the spectrum. To dissuade bias in interpretation of the individual contributions, it is worth noting that these same poles outside this range may generate slower component non-zero fluctuations. In turn, for a different range, these superimposed slower component fluctuations may provide the background level to resonances generated from other poles. Therefore, any particular pole may contribute either sharp or broad features for different parts of the spectrum.

2.9.2 Effects of the surroundings and particle absorption

Now attention is turned to the effect of the surrounding medium on the scattering efficiency of a BTO sphere with $n_s = 1.9$. Figure 2.9.2 plots the scattering

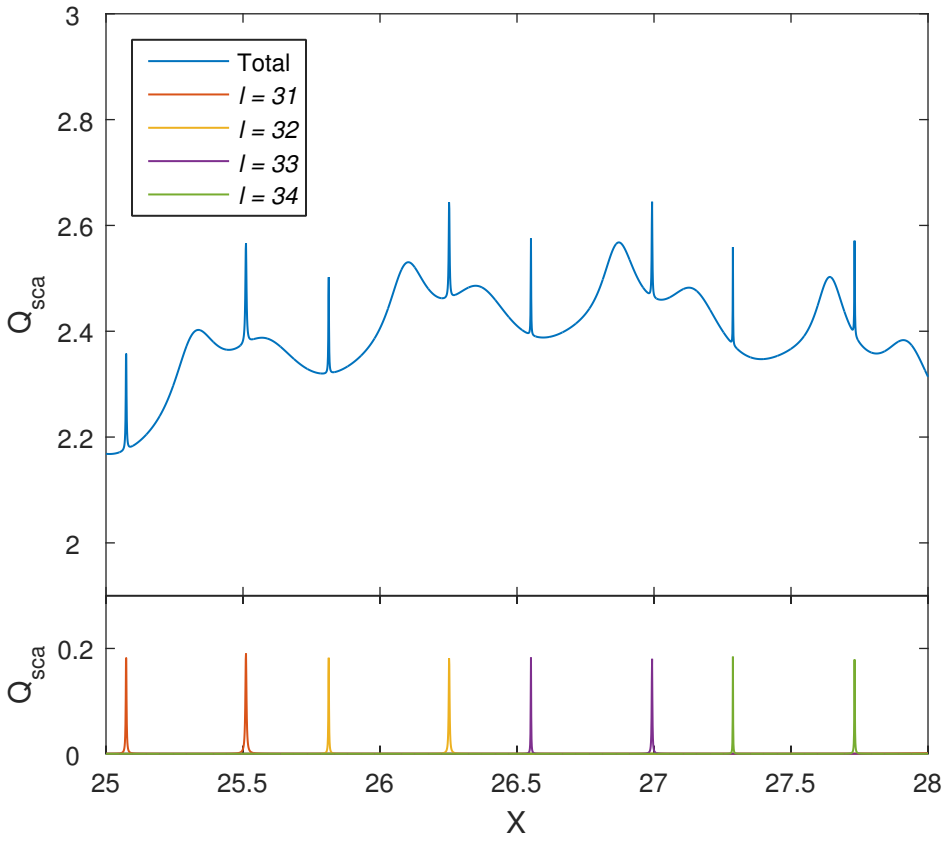

Figure 2.9.1: The scattering efficiency Q_{sca} of a sphere is obtained as a summation of contributions from individual multipoles. Individual multipole orders are seen to exhibit resonant effects that manifest as spectral peaks. (Above) Scattering efficiency Q_{sca} showing the total pole contribution summed from $l = 1$ to $l = 50$. (Below) Individual contributions from pole orders $l = 31, 32, 33$, and 34.

efficiency versus size parameter ranging from $x = 0$ to $x = 40$ for increasing values of the surrounding index $n_M = 1.3, 1.4, 1.5$, and 1.6. The behavior of spectral resonances is affected by changes in the surrounding index in a predictable manner. Namely, as the index of the host medium increases, the refractive index difference between the particle and its surroundings decreases. As the refractive index difference falls, less scattering and absorption occurs, so net dampening of resonances and feature broadening are observed. The choice of high-index

sphere helps to guard against resonance damping that happens as the surrounding index approaches closer to the particle index. In the important case for a sphere embedded in water, Figure 2.9.2 indicates that resonances are readily achievable.

The effect of raising the index of the surrounding medium was seen to increasingly dampen the spectral resonances. Scattering efficiency is also affected when the absorption in the sphere is changed. So far, the sphere index n_s has been assumed to be real. The effect of absorption can be included by specifying the imaginary index value of the sphere κ. Assuming time-dependence $e^{-i\omega t}$, a positive κ results in absorption for $n_s = 1.9 + i\kappa$. Figure 2.9.3 plots the scattering efficiency versus size parameter ranging from $x = 0$ to $x = 40$ for increasing values of the imaginary index value $\kappa = 10^{-4}, 10^{-3}, 10^{-2}$ and 10^{-1}. For $\kappa = 10^{-4}$ in Figure 2.9.3(a) and $\kappa = 10^{-3}$ in Figure 2.9.3(b), the resonances are still prominent. But increasing to $\kappa = 10^{-2}$ as in Figure 2.9.3(c) shows remarkable damping of previously sharp peaks. Increasing even more to $\kappa = 10^{-1}$, Figure 2.9.3(d) makes it obvious that the sphere can no longer sustain resonances and the spectrum of Q_{sca} smooths out considerably for $x > 10$.

In conclusion, MDRs are best enhanced for a low loss sphere with high index contrast compared to the surrounding medium.

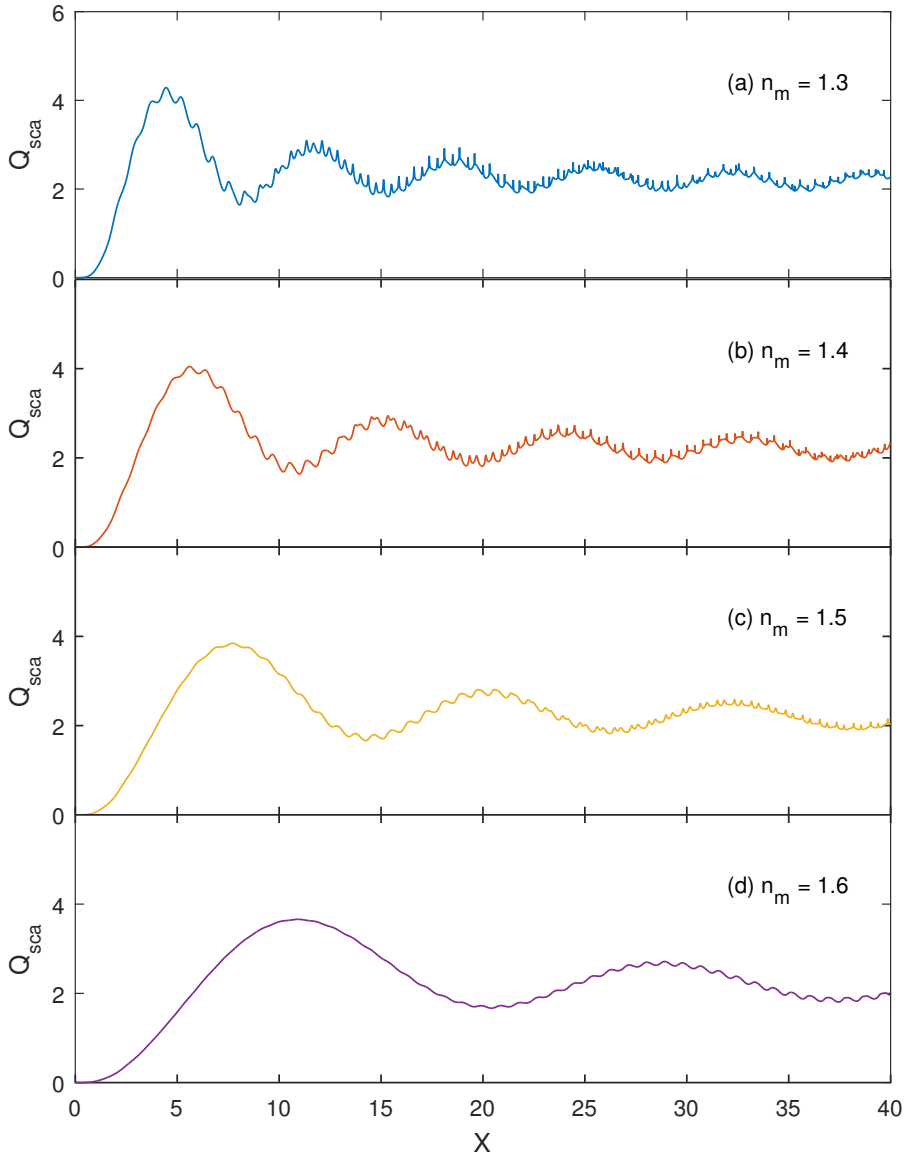

Figure 2.9.2: Scattering efficiency of a sphere with $n_s = 1.9$ for different index surrounding media

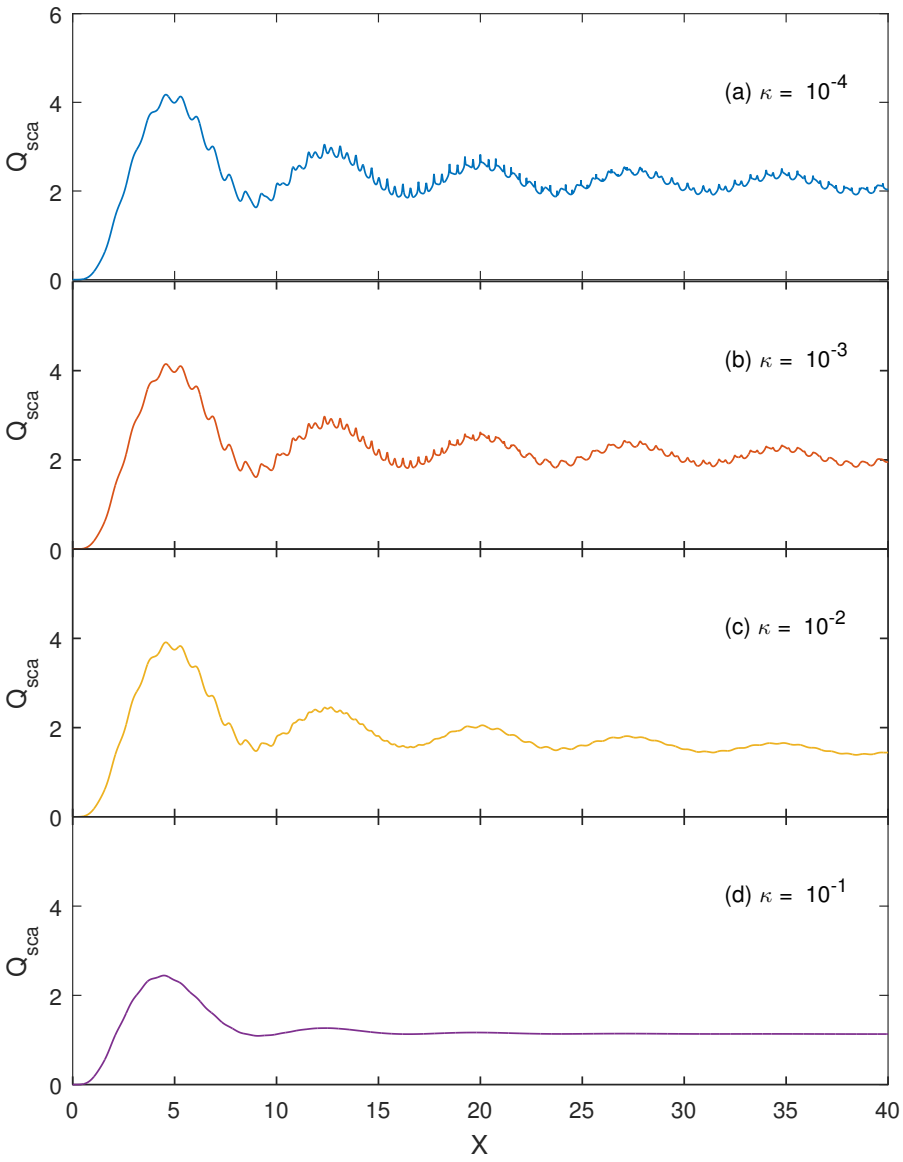

Figure 2.9.3: Scattering efficiency of a sphere in water with $n_s = 1.9 + i\kappa$ for different imaginary index values

2.10 Evanescent wave excitation of a sphere

Evanescent waves are experimentally important for their ability to transfer electromagnetic energy between one waveguide to another and between waveguides and resonators. The behavior of coupling energy to a sphere is of particular interest. Mie theory was shown to provide a good understanding of particle-light interaction for the plane wave case, now the interaction is explored for excitation of a sphere by an evanescent wave [89, 90, 91, 86].

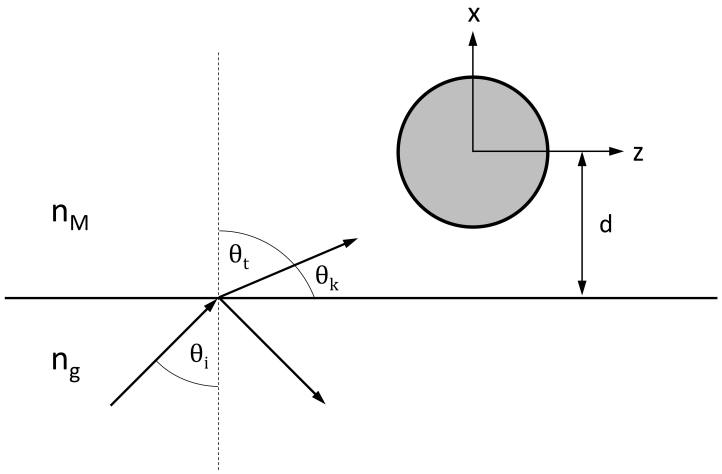

Figure 2.10.1: Evanescent wave excitation of a sphere

A schematic of the problem is given in Figure 2.10.1. As in Figure 1.6.1, the basic configuration is a dielectric interface with lower-index medium above and higher-index medium below. A dielectric sphere is added inside the lower-index medium of the top half-space. To facilitate comparison to the plane wave case and forthcoming experiments, refractive indices of the sphere and surrounding

medium are respectively recalled as $n_s = 1.9$ and $n_M = 1.33$. The bottom half-space is given the refractive index $n_g = 1.45$. The critical angle for this arrangement is $\theta_c = 66.5^{\circ}$. Light incident at this angle generates a plane wave which travels parallel to the interface. However, when light is incident at an angle exceeding the critical angle, total internal reflection (TIR) occurs. The result is an evanescent wave whose magnitude decays perpendicular to the the interface and moves parallel to the interface in medium 2. For incident angles steeper than the critical angle, the refracted angle becomes complex. Specifically, $\cos\theta_k < 1$ and $\sin\theta_k$ becomes purely imaginary. Therefore, unlike for an incident plane wave, an evanescent wave excitation results in angular terms of $\Pi_{l,m}, \mathrm{T}_{l,m} \geq 1$ and polarization-dependent expressions for the particle cross sections. Contributions from Legendre polynomials $P_{l,m}$ with $m \neq \pm 1$, not occurring from standard Mie theory, must be admitted. The expansion coefficients of the incident wave are [91, 86]

$$\alpha^s_{TM}(l,m) = 2i^n n_M \left[\frac{\pi(2l+1)(l-m)!}{l(l+1)(l+m)!}\right]^{\frac{1}{2}} \frac{mP_{lm}(\cos\theta_k)}{\sin\theta_k} E^s_t \tag{2.10.1}$$

$$\alpha^s_{TE}(l,m) = 2i^{n+1} \left[\frac{\pi(2l+1)(l-m)!}{l(l+1)(l+m)!}\right]^{\frac{1}{2}} \frac{dP_{lm}(\cos\theta_k)}{d\theta_k} E^s_t \tag{2.10.2}$$

for an s-polarized incident wave and

$$\alpha_{TM}^{p}(l,m) = 2i^{n+1}n_M \left[\frac{\pi(2l+1)(l-m)!}{l(l+1)(l+m)!}\right]^{\frac{1}{2}} \frac{dP_{lm}(\cos\theta_k)}{d\theta_k} E_t^p \tag{2.10.3}$$

$$\alpha_{TE}^{p}(l,m) = -2i^{n} \left[\frac{\pi(2l+1)(l-m)!}{l(l+1)(l+m)!}\right]^{\frac{1}{2}} \frac{mP_{lm}(\cos\theta_k)}{\sin\theta_k} E_t^p \tag{2.10.4}$$

for a p-polarized incident wave. In each case, E_t is the complex amplitude of the refracted wave's electric field vector found via Fresnel's equations. The expression of scattered fields may be set up using expansion coefficients $\beta_{TM}^{s,p}(l,m)$ and $\beta_{TE}^{s,p}(l,m)$, and internal fields can be represented similarly. Applying appropriate boundary conditions at the surface of the sphere results in the scattering coefficients of the sphere, given as

$$\beta_{TM}^{s,p}(l,m) = a_l \alpha_{TE}^{s,p}(l,m) \tag{2.10.5}$$

$$\beta_{TE}^{s,p}(l,m) = b_l \alpha_{TM}^{s,p}(l,m) \tag{2.10.6}$$

where a_l and b_l are the scattering coefficients of standard Mie theory from section 2.7. Cross-sections for extinction and scattering from subsection 2.8.1 are recalled with modifications to the angular functions that now also depend on the order l.

$$\sigma_{ext}^{s} = \frac{2\pi}{k_M^2}\frac{1}{N}\sum_{l=1}^{\infty}(2l+1)\mathrm{Re}\left\{a_l\Pi_l + b_n\mathrm{T}_n\right\} \tag{2.10.7}$$

$$\sigma_{sca}^{s} = \frac{2\pi}{k_M^2}\frac{1}{N}\sum_{l=1}^{\infty}(2l+1)\left(\left|a_l\right|^2\Pi_l + \left|b_l\right|^2\mathrm{T}_l\right) \tag{2.10.8}$$

for s-polarized light and

$$\sigma_{ext}^{p} = \frac{2\pi}{k_M^2}\frac{1}{N}\sum_{l=1}^{\infty}(2l+1)\mathrm{Re}\left\{|a_l|^2\,\mathrm{T}_l + |b_l|\,\Pi_l^2\right\} \tag{2.10.9}$$

$$\sigma_{sca}^{p} = \frac{2\pi}{k_M^2}\frac{1}{N}\sum_{l=1}^{\infty}(2l+1)\left(a_l\mathrm{T}_l + b_l\Pi_l\right) \tag{2.10.10}$$

for p-polarized light, with definitions of the Mie angular functions

$$\Pi_l = \frac{2}{l(l+1)}\sum_{m=-l}^{l}\frac{(l-m)!}{(l+m)!}\left|m\frac{P_{lm}(\cos\theta_k)}{\sin\theta_k}\right|^2 \tag{2.10.11}$$

$$\mathrm{T}_l = \frac{2}{l(l+1)}\sum_{m=-l}^{l}\frac{(l-m)!}{(l+m)!}\left|m\frac{dP_{lm}(\cos\theta_k)}{d\theta_k}\right|^2 \tag{2.10.12}$$

The normalization factor N that appears in the cross-sections is unity for plane waves but is different for evanescent waves. This difference arises from the exponentially decaying field which creates a non-uniform energy flux across the cross-section. A useful normalization for evanescent waves is to normalize with respect to the total power incident on the particle. This definition avoids diverging efficiencies for large particles where the intensity approaches zero at the particle center. The normalized intensity is taken as the incident intensity averaged over the particle's cross-sectional area perpendicular to the Poynting vector of the evanescent wave:

$$\tilde{I}_0 = \frac{1}{\pi R^2}\int\int \mathbf{S_{inc}}\cdot\mathbf{n}dA = I_0\exp(-2\kappa d)\frac{n_s}{n_M}\sin\theta_i\frac{I_1(2\kappa R)}{\kappa R} \tag{2.10.13}$$

where $I_1(2\kappa R)$ is the modified Bessel function of the first kind of order 1 and argument $2\kappa R$. Denoted by κ is the attenuation constant

$$\kappa = k_M\sin\theta_k = \frac{2\pi}{\lambda}\sqrt{n_s^2\sin^2\theta_i - n_M^2} \tag{2.10.14}$$

which is defined essentially as the inverse of the penetration depth. For the sketched model, at a distance d away from the interface there is decrease in the field magnitude by a factor $\exp(-\kappa d)$ from its value at the interface. In comparison, the field intensity proportional to the field amplitude squared decays by a factor $\exp(-2\kappa d)$ which is the behavior apparent from 2.10.13. The normalization for evanescent excitation is identified from 2.10.13 as

$$N = \frac{n_s}{n_M} \sin\theta_i \frac{I_1(2\kappa R)}{\kappa R} \tag{2.10.15}$$

Having specified the normalization factor, the cross-sections for evanescent waves are completely specified. Dimensionless efficiency factors can be formed by further dividing the cross-sections by the geometrical cross-section σ_{geo} given as πR^2 for a sphere of radius R. The behavior of efficiencies for evanescent waves follows and is compared against the behavior of efficiencies for plane waves.

For incident angles exceeding the critical angle, the wavevector component $k_M \sin\theta_k$ becomes imaginary causing the electromagnetic field to exponentially decay away from the interface. When the distance d is small enough, the sphere can intercept energy from the evanescent wave that penetrates into the top half-space of medium 2. In Figure 2.10.2, the scattering efficiency for an incident plane wave is compared to an incident TE evanescent wave. The evanescent wave is considered to have been generated by plane wave after TIR from an interface as shown in Figure 2.10.1 with $n_g = 1.45$ and $n_M = 1.33$. Incident angles of $70°, 75°$, and $80°$ are considered for which a pattern of strengthened resonances is

clearly observed for steepening incidence. This results from the enhancement of high order multipoles caused by the evanescent wave which magnifies for increased angles.

Figure 2.10.3 makes the same comparison for the near field efficiency for which the same trend occurs. Evanescent waves generated from more steeply approaching plane waves at an interface result in enhanced high order multipoles. In turn, this strengthens resonances in the observed near field efficiency.

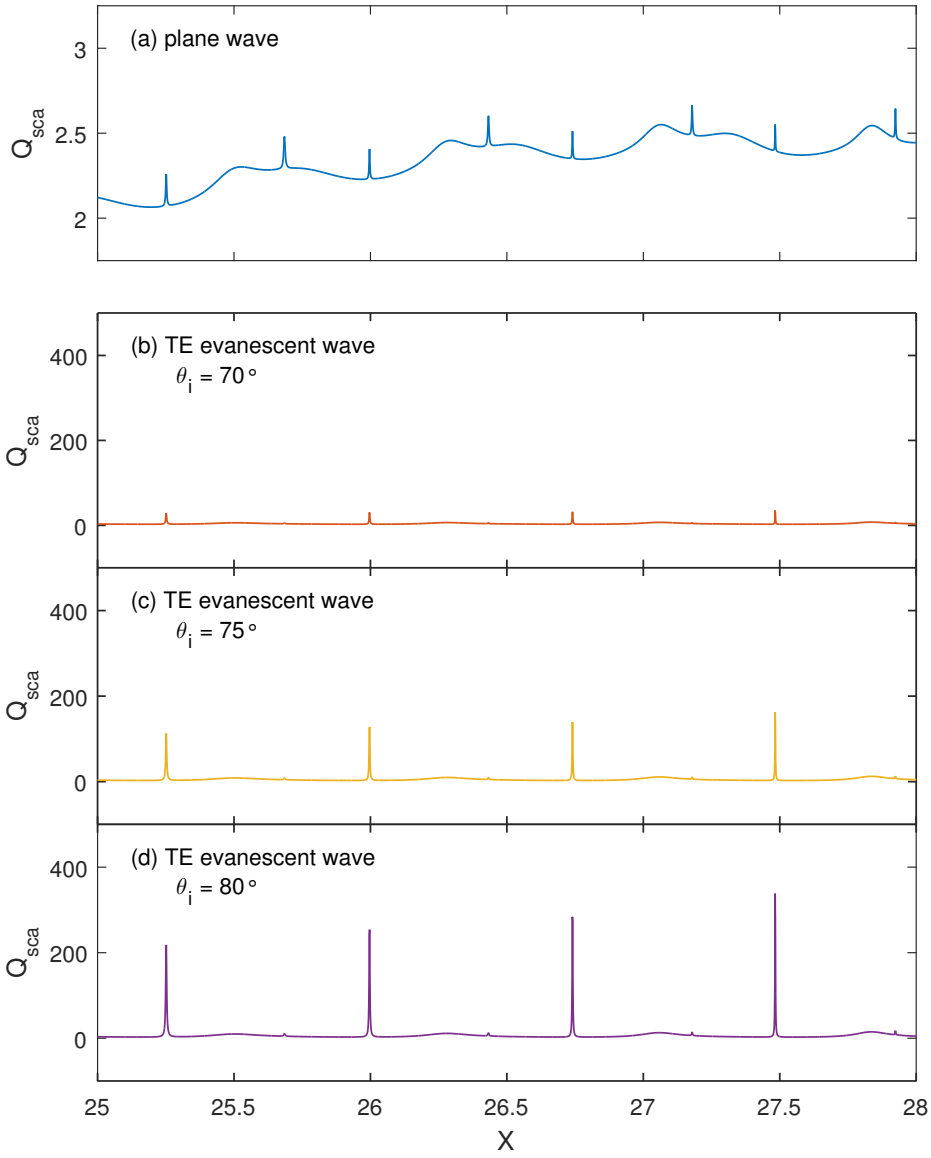

Figure 2.10.2: Scattering efficiency is compared for an incident plane wave and incident TE evanescent wave. The evanescent wave is generated by a plane wave after TIR from an interface as shown in Figure 2.10.1 with $n_g = 1.45$ and $n_M = 1.33$. Incident angles of $70°, 75°$, and $80°$are considered. Steeper incidence shows greater resonance enhancement. Steeper incidence shows greater resonance enhancement due to contributions from high order multipoles that occur for evanescent waves.

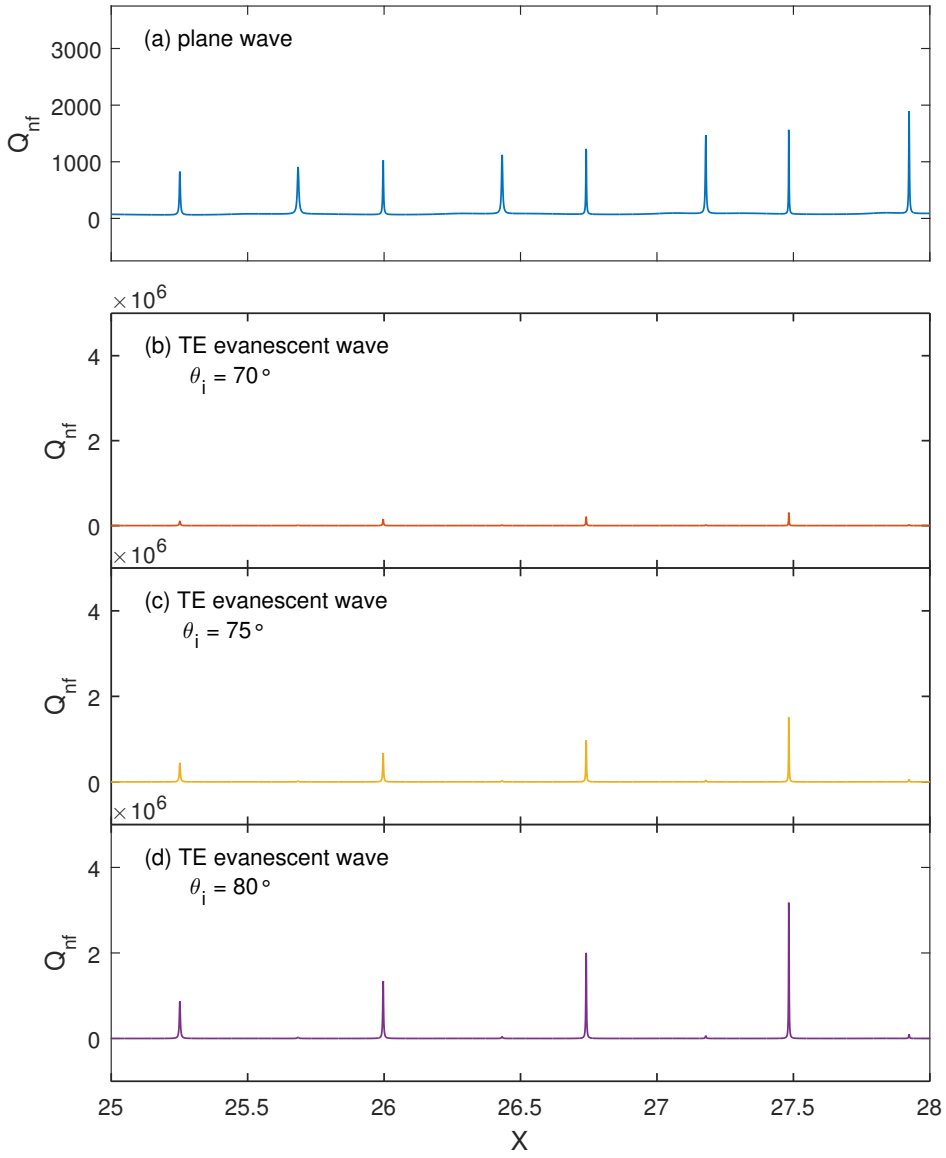

Figure 2.10.3: Near field efficiency is compared for an incident plane wave and incident TE evanescent wave. The evanescent wave is generated by a plane wave after TIR from an interface as shown in Figure 2.10.1 with $n_g = 1.45$ and $n_M = 1.33$. Incident angles of $70°, 75°$, and $80°$are considered. Steeper incidence shows greater resonance enhancement due to contributions from high order multipoles that occur for evanescent waves.

Chapter 3

Fabrication methods

Fabrication of the optical fiber microstructures consists of glass fiber etching procedures followed by a press fit insertion of size-matched spherical resonators. Oxide glasses are well known to dissociate in solutions of hydrofluoric (HF) acid. HF acid is a selective etching agent that dissolves different oxide materials at different rates. Advantages of chemical etching include mass production, high reproducibility, and tailored fiber sculpting by proper control of the etch conditions. Furthermore, the method is amenable to industrial fabrication. For glass optical fibers whose core and cladding possess different levels of oxide dopants, the cylindrical profile of the core can either be carved out to make a pocket or sharpened to a point [92, 93]. Experiments demonstrate that in unbuffered HF acid the dissolution rate of the germanium dioxide (GeO_2) doped silica fiber core is faster than that of the pure silica cladding, so that the end of the fiber core becomes concave. To lower the dissolution rate, ammonium fluoride (NH_4F) can

be added to HF as a buffer solution to tune the etching selectivity. At a specific ratio, a reversal in etching selectivity occurs [93].

Two standard commercial etchants used here are hydrofluoric (HF) acid solution (49% w/w) and 6:1 buffered oxide etchant (BOE) (40% NH_4F : 49% HF, both concentration w/w). HF acid and BOE demonstrate opposite etching selectivity. The effect of this reversal in selectivity is related to the ratio of NH_4F to HF. Generally, HF acid dissolves higher doped regions more quickly than lesser doped regions. In contrast, BOE dissolves lesser doped regions faster than higher doped regions. The selectivity of the etchants motivates the order, duration, and reason for their use. The design of an etched fiber structure considers both the choice of starting fiber and selectivities of the etchants. In practice, the etch procedure is tailored to the observed etching behavior of a particular fiber.

This work demonstrates etching procedures on several types of optical fiber. The starting optical fibers of choice here are all variations of polarization-maintaining fiber (PMF). A regular single-mode fiber (SMF) has its core doped with GeO_2 to raise the refractive index compared to the cladding. A PMF has two additional stress rods that flank the core on opposite sides. Highly doped, for instance with boron trioxide (B_2O_3), the stress rods thermally expand during fiber drawing to create internal stresses that induce optical anisotropy in the final product. In short, PMF is composed of three regions of silica glass classified by different doping concentration: an un-doped cladding, a doped core, and highly doped stress rods. The etching process was conceived to leverage these differences in dopant levels

to selectively etch the desired structure. Different procedures are developed for bow-tie fiber, reduced cladding panda fiber, and standard cladding panda fiber.

Bow-tie and panda fibers are both named according to approximate shape of their respective cross-sections. From the end-face of a bow-tie fiber, the stress rods look roughly like trapezoids that become more slender closer to the core. Taken altogether, the central core bordered by two slightly slender trapezoids appears like a "bow-tie." From the end-face of a panda fiber, the stress rods have circular cross-sections that are larger in proportion to the core. Therefore, this pattern of three circles with one smaller circle sandwiched between two larger circles appears like a "panda face." Cute terminology aside, the fibers allow for some interesting and functional etched microstructures.

The general motivation behind using types of PMF to etch is found in capability to rapidly etch pockets in the regions of the highly doped stress rods. For the purpose of building a fiber-integrated resonator, achieving a hollow inside the fiber in tangent location to the core is critical for efficient excitation. It has been found that the stress rods can be etched sufficiently fast that the core can be essentially preserved for input and output coupling of light. The geometry of the different fibers will be shown to demand different etch steps and durations, but the final goal is the same. Specifically, the fibers are etched in a manner consistent with providing robust support for a spherical resonator in adequate position for exciting WGMs. This section will continue with a description and explanation of the fabrication methods and fabrication results for each fiber individually. Notably,

all etching procedures are performed at room temperature (25°C).

A unique aspect of the press fit fiber microstructures to be described is the capability to incorporate a resonator without use of a three-axis translations stage or micro-manipulation of a single sphere. The shared technique of these structures requires only pressing the etched fiber into a vial of size-matched spheres suspended in isopropanol (IPA). The spheres used here (Corpuscular Inc.) are monodisperse beads made from barium titanate (BTO) of refractive index ~1.9. Further details regarding press-fitting and sphere dimensions are given in the case of each fiber structure.

3.1 Bow-tie fiber (BTF)

BTF (Fibercore HB1500) is etched in a two-step process. In preparation, a BTF stub is made by standard arc-splicing BTF to an SMF pigtail and cleaving the BTF to a convenient length $>100\mu m$. As is common for these microstructures, the absolute length of the fiber stub is arbitrary but a lower limit is incurred. The lower bound is set to a length greater than the final etch depth inside the fiber as found from experimentation. Having prepared the BTF stub, it is first immersed in HF acid solution (49% w/w) for $3min$. The HF acid rapidly etches deep pockets into the stress rods (Figure 3.1.1). The inward procession of the etchant into the fiber end-face produces gradually narrowing channels. The BTF used here has stress rods tightly positioned by the core. Therefore, to preserve the

core for excitation, such a short etch time is mandatory. The concave inner surface of the stress rods for BTF well approximates the curvature of the core, so even as the etchant encroaches inwards from the hollowed stress rods the basic cylindrical cross-section of the core remains (Figure 3.1.2). Between etch steps, the fiber stub is flushed with deionized (DI) water and dried with compressed nitrogen. In the second etch step, the fiber stub is immersed in 6:1 BOE for $30min$. With reversed etch selectivity to HF, BOE effectively widens the pockets by attacking the undoped cladding and gradually thins the core from all sides to form a free-standing needle-shaped taper (Figure 3.1.4). To terminate etching, the fiber stub is again flushed with DI water and left to dry under ambient conditions.

To complete the BTF press fit resonator, a sphere must be inserted. A sphere can be captured by dipping a press fit BTF into an IPA suspension of spheres with diameter $\sim 29\mu m$. Figure 3.1.4 shows the end-face with taper illumination by He-Ne laser and a $29\mu m$ sphere press fit into position. The sphere is held in place between the taper core and silica housing provided by the etched cladding. In tangent contact with the taper core, the sphere is in good placement for excitation of WGMs, but its position is not the most secure. While a sphere of slightly larger dimension might fit more snugly, the $\pm 1\mu m$ diametric tolerance of the spheres at this range interferes with consistency. Proceeding fiber microstructures will seek to address the security of the sphere inside the fiber while preserving a position for practical light coupling.

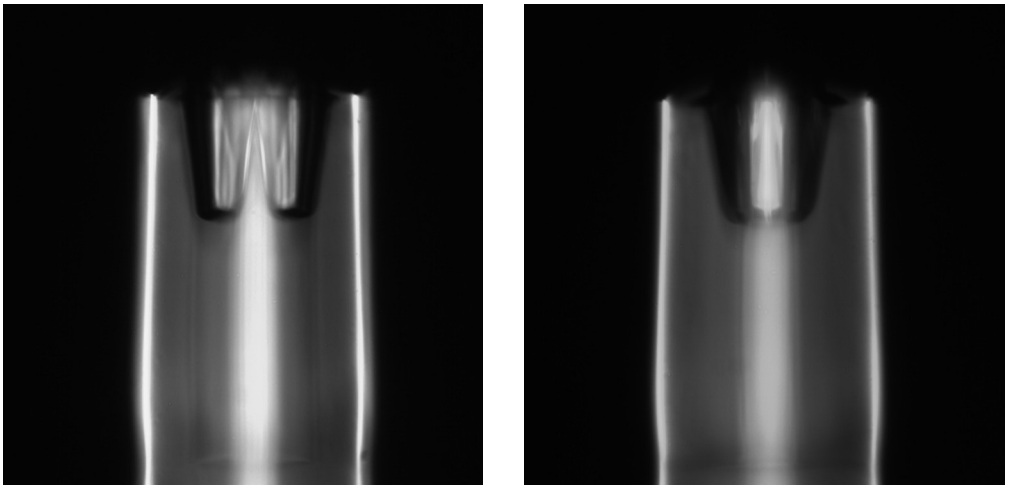

(a) (b)

Figure 3.1.1: Side view microscope images for 3*min* HF etch of BTF. (a) View of hollowed stress rods. (b) View of single pocket with silhouette of etched core.

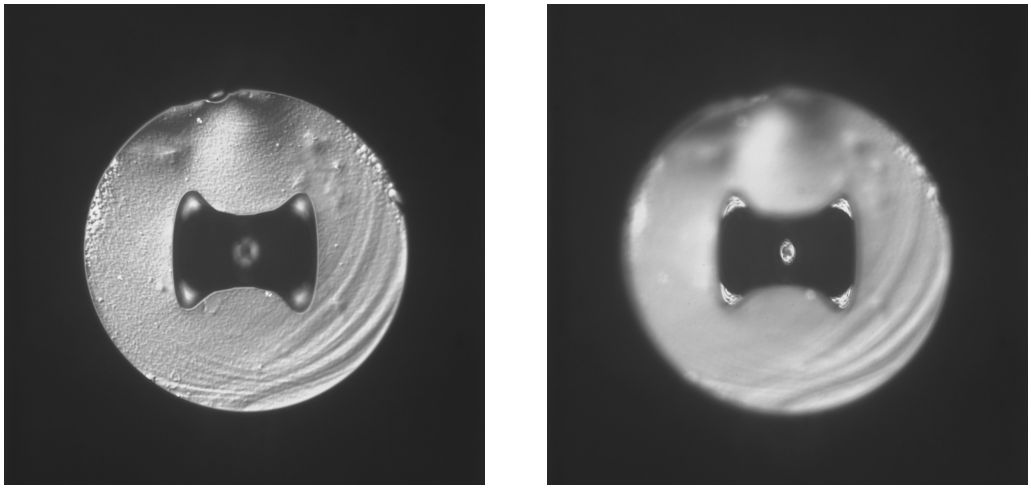

(a) (b)

Figure 3.1.2: End-face view microscope images for 3*min* HF etch of BTF. (a) End-face in focus. (b) Core in focus.

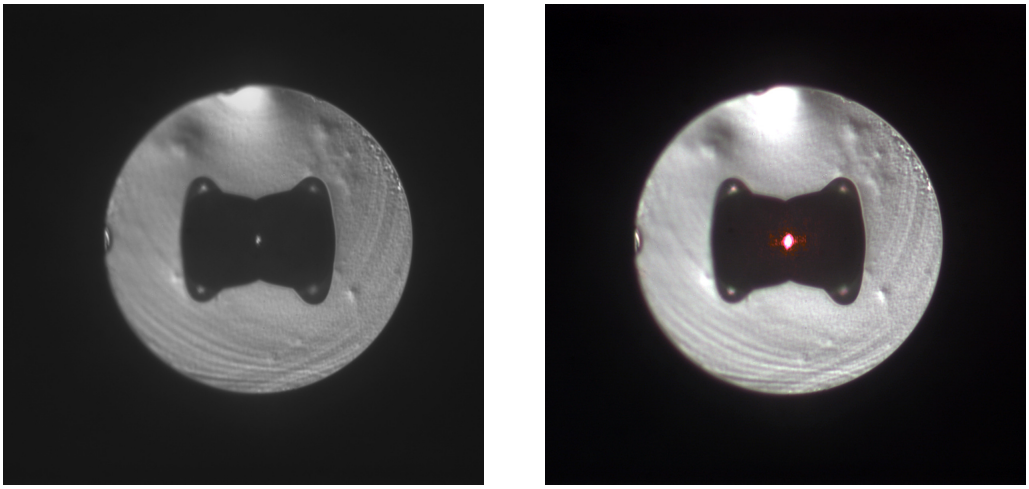

(a) (b)

Figure 3.1.3: End-face view microscope images for $3min$ HF / $30min$ BOE etch of BTF. (b) End-face in focus. (c) End-face with taper illumination by He-Ne laser

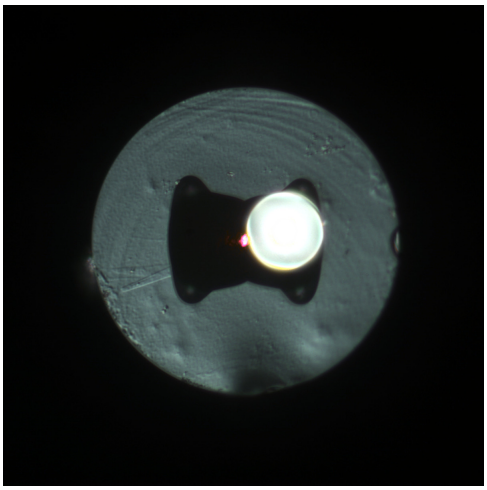

Figure 3.1.4: End-face view microscope image of BTF press fit resonator. Sphere with ~$29\mu m$ diameter inserted into BTF with taper illumination by He-Ne laser.

3.2 Reduced cladding panda fiber (RC-PMF)

RC-PMF is panda PMF with a cladding diameter of $80\mu m$. The dimensions and positioning of the circular stress rods of RC-PMF are similar to BTF. An analogous two-step etch process for RC-PMF is $2min$ in HF and $50min$ in BOE.

Figure 3.2.1 shows side view microscope images of RC-PMF after a $2min$ HF etch. Corresponding end-face view microscope images are given in Figure 3.2.2 showing that the hollowed stress rods form two deep pockets aligned next to the core. Importantly, each pocket made in the fiber has a circular cross-section, thereby providing a natural slot for a spherical resonator to be inserted. An advantage exists to etch the cladding to the point of breach. The reasons are briefly reserved until discussion of the assembly. To ensure a cladding breach of the final structure along the diameter through the slow axis of the RC-PMF, an additional etch step in BOE is added to the beginning. Therefore, the etch procedure for RC-PMF becomes three steps: $30min$ etch in BOE, $2min$ etch in HF, then $50min$ in BOE.

In preparation, an RC-PMF stub is made by arc-splicing RC-PMF to an SMF pigtail and cleaving the RC-PMF to a convenient length $>100\mu m$. Again, the absolute length of the fiber stub is arbitrary but a lower limit is set greater than the final etch depth in the fiber. The first etch step, $30min$ in BOE, merely thins the already reduced cladding which will breach completely in the third step. Between etch steps, the fiber stub is flushed with DI water and dried with compressed nitrogen. The second step, $2min$ in HF acid, rapidly etches deep pockets into the stress rods (Figure 3.2.1) and pinches inward on the core (Figure 3.2.2). End-face views in Figure 3.2.2 show the etched pockets are circular in cross-section. The etched channels narrow deeper inside the fiber so that the three-dimensional shape of either pocket is a cone frustum. Between etches, the fiber stub is again flushed and dried. In the third etch step, the fiber stub is immersed in BOE for $50min$

(Figure 3.2.3). BOE opens the pockets further by etching the un-doped cladding and slowly tapers the core (Figure 3.2.4). To finish, the fiber stub is flushed clean and allowed to dry under ambient conditions. To complete assembly of the RC-PMF press fit resonator, a sphere must be inserted. A resonator can be captured by dipping the fiber stub into a vial of ~29μm spheres. The sphere is mated inside the cone frustum pocket in tangent contact with the taper core. The sphere placement is conducive for WGM excitation and more robust than the position offered by the BTF press fit resonator. Figure 3.2.5 shows the end-face with taper illumination by He-Ne laser and a ~29μm sphere press fit into position. The advantage of the breached cladding can be understood that light coupled to WGMs will circulate unimpeded around the sphere circumference.

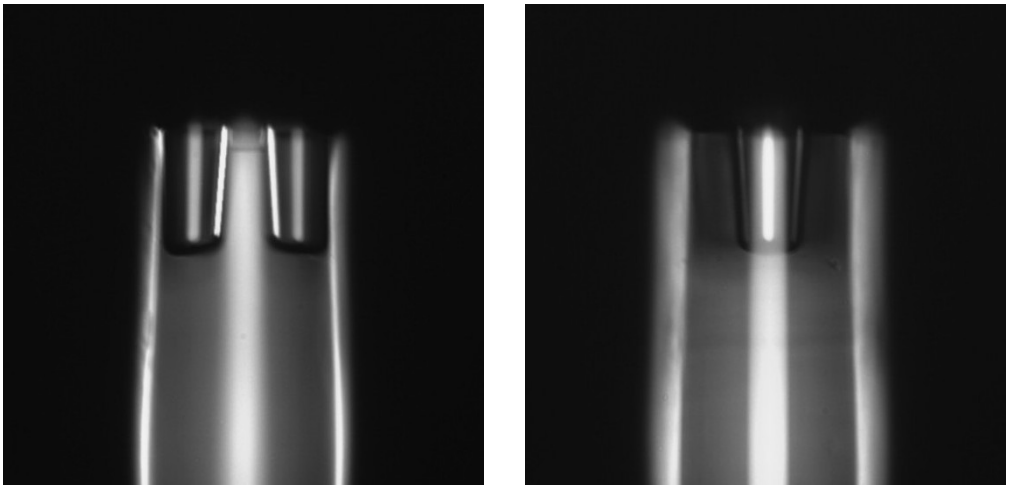

(a) (b)

Figure 3.2.1: Side view microscope images for 2min HF etch of RC-PMF. (a) View of hollowed stress rods. (b) View of single pocket.

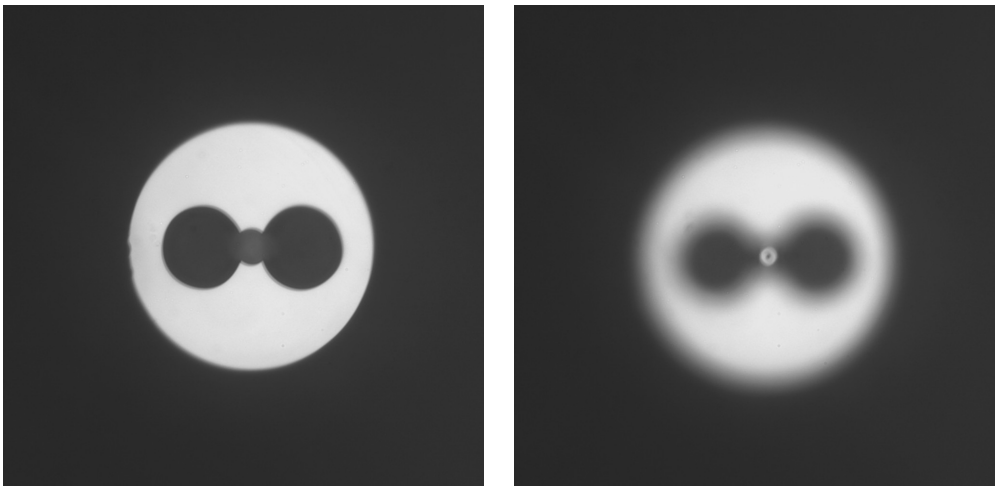

(a) (b)

Figure 3.2.2: End-face view microscope images for $2min$ HF etch of RC-PMF. (a) End-face in focus. (b) Core in focus.

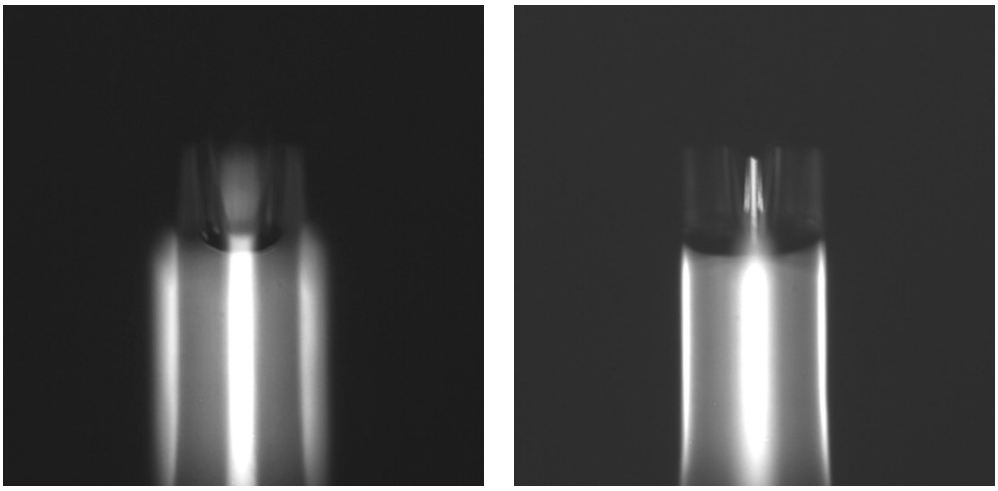

(a) (b)

Figure 3.2.3: Side view microscope images for $30min$ BOE/ $2min$ HF / $50min$ BOE etch of RC-PMF. (a) View through breached cladding into a pocket. (b) View of taper core in focus.

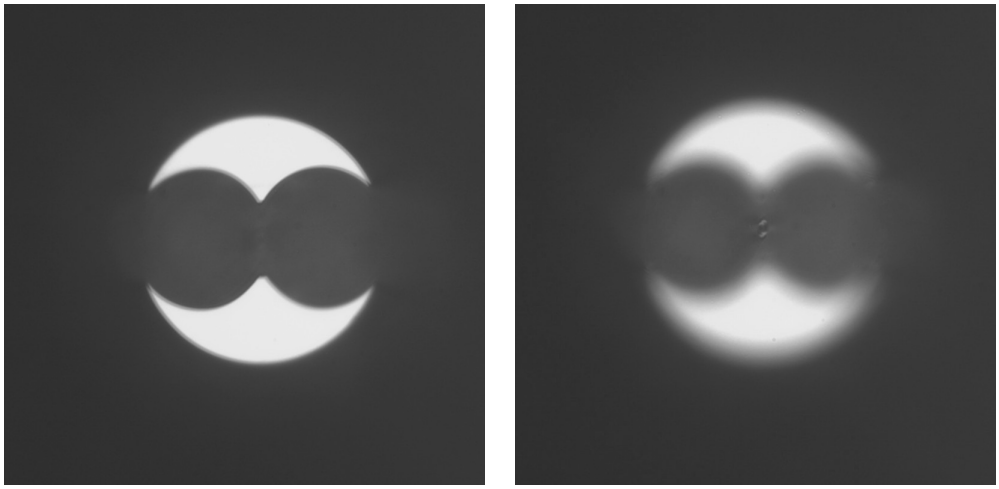

(a) (b)

Figure 3.2.4: End-face view microscope images for $30min$ BOE/ $2min$ HF / $50min$ BOE etch of RC-PMF. (b) End-face in focus. (c) Core taper in focus

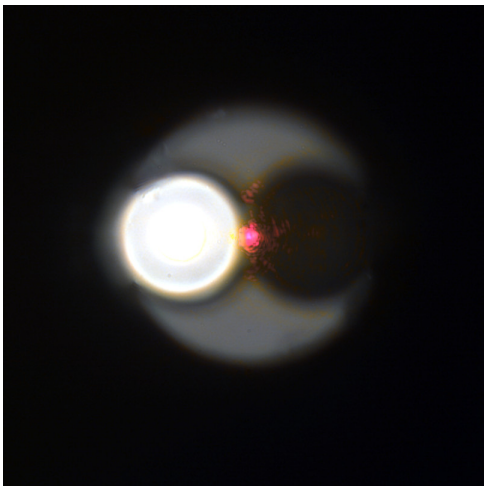

Figure 3.2.5: End-face view microscope image of RC-PMF press fit resonator. Sphere with ~$29\mu m$ diameter inserted into RC-PMF with taper illumination by He-Ne laser.

3.3 Standard cladding panda fiber (SC-PMF)

SC-PMF is panda PMF with a standard cladding diameter of $125\mu m$. A sample is initially prepared by standard splicing PMF to an SMF pigtail and cleaving the PMF to a length of $>60\mu m$. The absolute length of PMF is arbitrary, but a lower limit is incurred by the final etch depth of the stress rods. The length used here was approximately $120\mu m$ achieved via a micrometer-mounted cleaver. Wet chemical etching was performed by direct immersion of the PMF stub into etching solution. Two standard commercial etchants used for processing the PMF were hydrofluoric (HF) acid solution (49% w/w) and 6:1 buffered oxide etchant (BOE) (40% NH_4F : 49% HF, both concentration w/w). Etching procedures all take place at room temperature (25°C). In the first step, the PMF stub is immersed into HF acid for $3min$. Afterwards, the sample is flushed with DI water and dried using compressed nitrogen. In the second step, the PMF stub is immersed into BOE for $60min$. The sample is again flushed clean with DI water and allowed to dry under ambient conditions.

HF acid and BOE have opposing etching selectivities due to the ratio of NH_4F to HF [93]. HF acid dissolves higher doped regions more quickly than lesser doped regions, while BOE shows the opposite behavior. Therefore, etchant selectivity motivates the order, duration, and reason for their use. First, in the period of a few minutes, HF acid aggressively etches away the stress rods (Figure 3.3.1) and encroaches slightly upon the core (Figure 3.3.2). Second, over the span of an

hour, BOE gradually shapes the final flat-blade taper core and widens the pockets finally breaching the cladding. The longer etch time of BOE allows for controlled etching of the taper without significant surface degradation. Figure 3.3.3 gives side views of the etched PMF microstructure showing the hollowed stress rods and flat-blade taper core. The etching ingress depth of either pocket is ~$54\mu m$. With its tip set back slightly from the face, the taper length is ~$50\mu m$. The taper apex angle is estimated as $2\arctan\left[(0.5)\left(7\mu m\right)/50\mu m\right] = 8.0°$.

After etching, the microstructure is ready to receive a sphere (Figure 3.3.4). The microsphere used here is $52\mu m$ in diameter, available as a monodisperse bead (Corpuscular Inc.). Made from barium titanate (BTO), the refractive index is ~1.9. The technique of integrating the sphere is to press the etched PMF directly into a vial of spheres dispersed in IPA. Quick and alignment-free, the action of press fitting a microsphere requires no manipulation of a three-dimensional translation stage or conveying of individual spheres. The shape and depth of a pocket allows only one sphere. Despite having two pockets, it is far more common to capture a single sphere due to the $\pm 1\mu m$ diametric tolerance of the spheres as received. Set back from the fiber end-face, the fiber taper is well protected while mating a sphere into a press fit position. Inward progress of the sphere inside the fiber is terminated by the gradually narrowing pocket such that the taper is the only contact point in the path of circulating light (Figure 3.3.5(a)). The pocket's circular-cross section guides a sphere into a secure pincer grip applied by the cladding protrusions (Figure 3.3.5(b)). To facilitate press-fitting of the sphere,

the reflection spectrum can be monitored simultaneously. Figure 3.3.6 shows the end-face with taper illumination by He-Ne laser and a ~$52\mu m$ sphere press fit into position. Fine detail of the SC-PMF press fit resonator is provided by the SEM image in Figure 3.3.7.

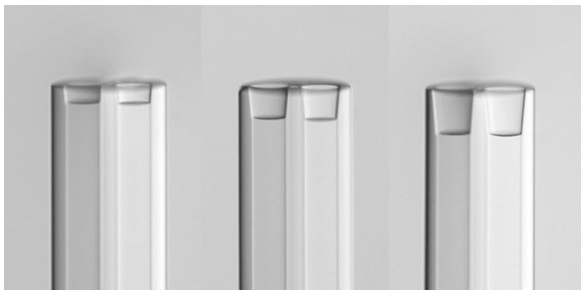

(a)

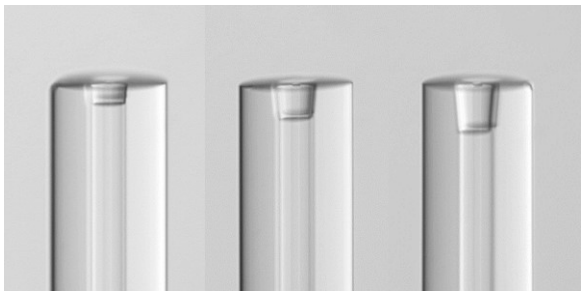

(b)

Figure 3.3.1: Side view microscope images when immersed in index matching fluid showing the evolution for 1, 2, 3min HF etch of SC-PMF. (a) View of two pocket side. (b) View of one pocket side.

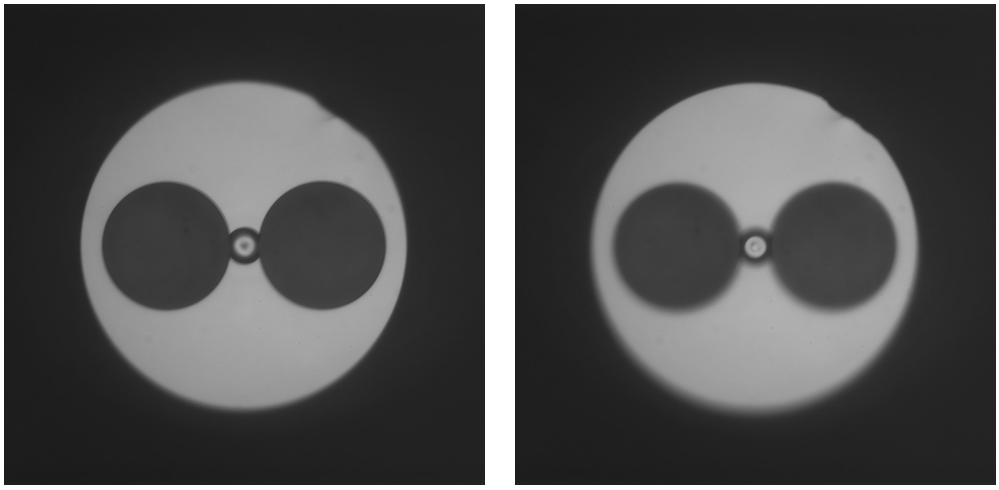

(a) (b)

Figure 3.3.2: End-face view microscope images for $3min$ HF of SC-PMF. (a) End-face in focus. (b) Core in focus.

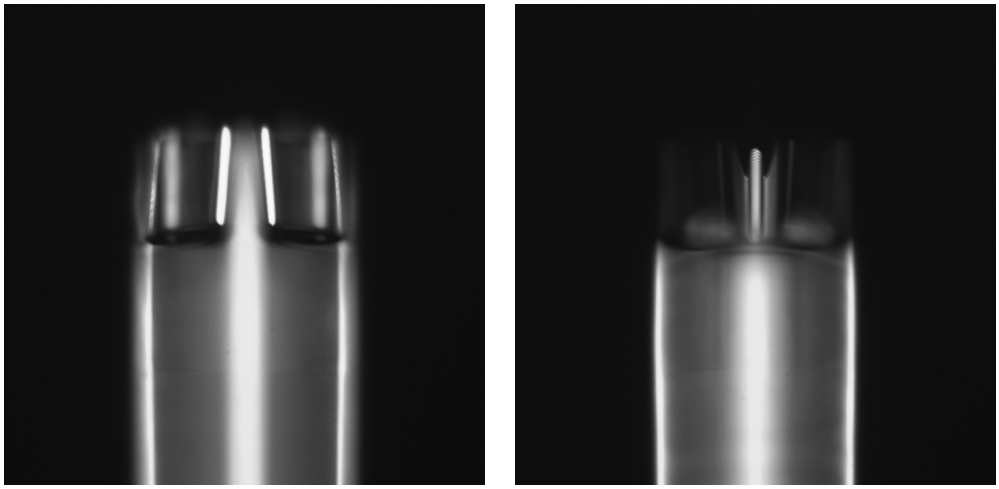

(a) (b)

Figure 3.3.3: Side view microscope images for $3min$ HF / $60min$ BOE etch of SC-PMF. (a) View of two pockets created from etched stress rods. (b) View through the breached pocket of the flat-blade taper core in focus.

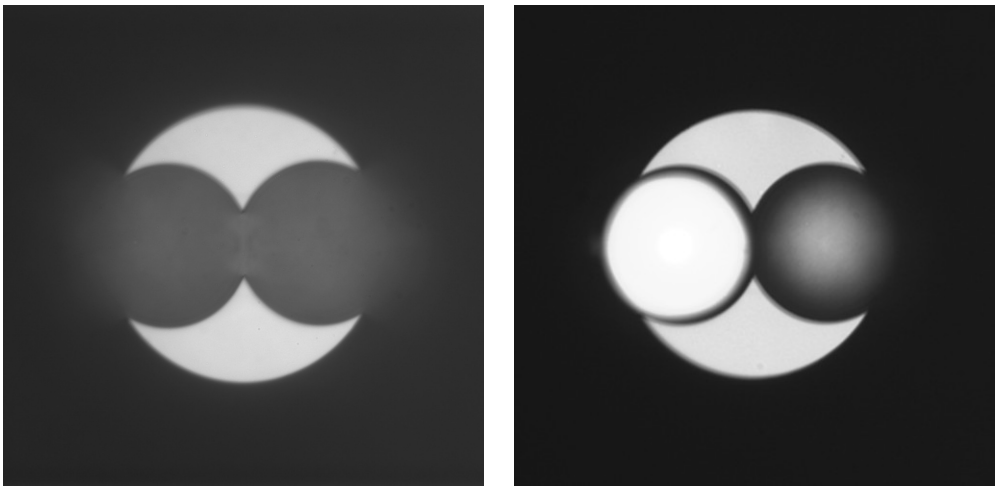

(a) (b)

Figure 3.3.4: End-face view microscope images for $3min$ HF / $60min$ BOE etch of SC-PMF. (b) End-face empty. (c) End-face with ~$52\mu m$ diameter sphere inserted in left pocket

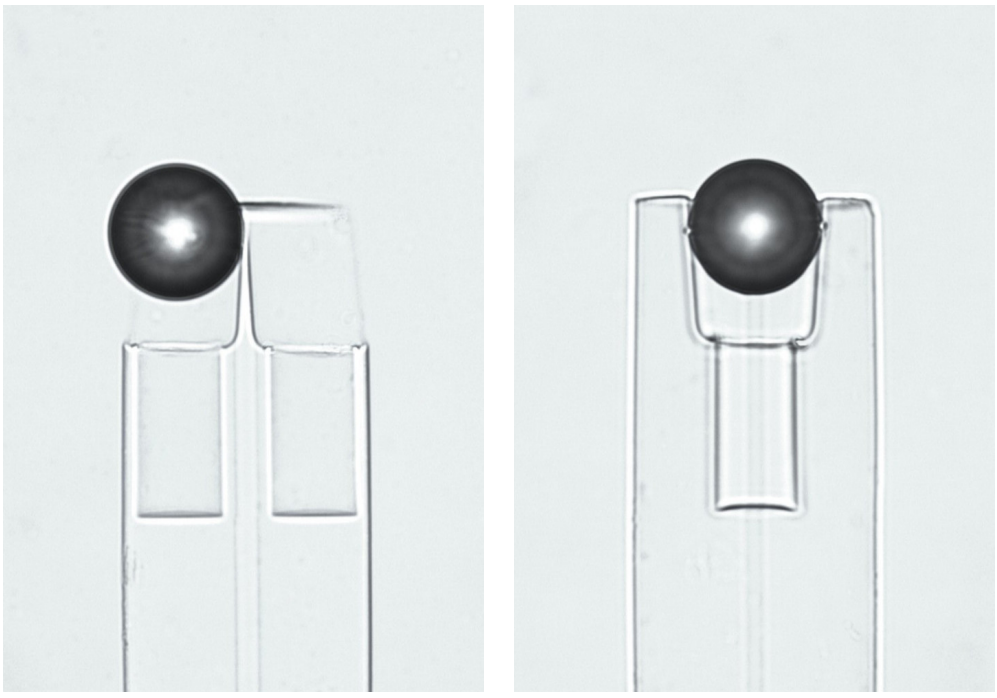

(a) (b)

Figure 3.3.5: Side view microscope images of SC-PMF press fit resonator when immersed in index matching fluid. Sphere with ~$52\mu m$ diameter inserted into SC-PMF

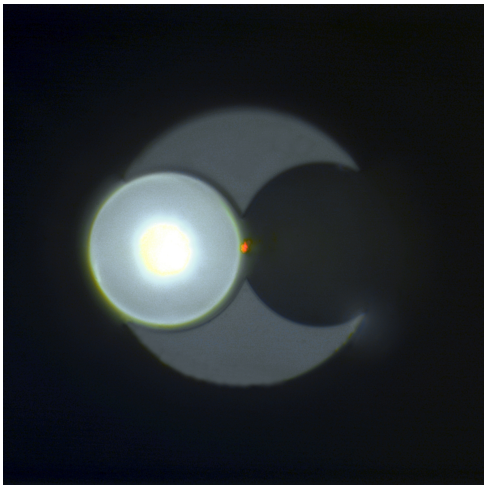

Figure 3.3.6: End-face view microscope image of SC-PMF press fit resonator. Sphere with ~52μm diameter inserted into SC-PMF with taper illumination by He-Ne laser.

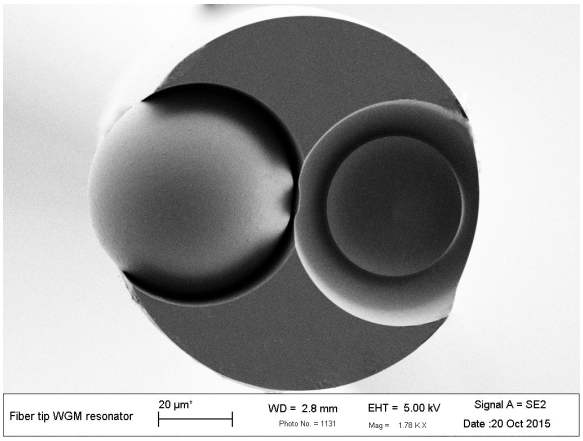

Figure 3.3.7: This scanning electron microscope image of an assembled SC-PMF press fit resonator shows fine detail of the inserted ~52μm diameter sphere in tangent contact with the flat-blade taper core.

Chapter 4

Experimental results

Fabrication procedures were given for three types of press fit spherical resonators. Reflection spectra for each type provide a useful gauge of their performance. Data was recorded for each press fit resonator while submerged in IPA and in DI water. An effect worth note is that a reflection spectrum in IPA demonstrates a background typically $4dB$ lower than a spectrum in DI water. Measurements were done using a component testing system (Micron Optics, si720), that features a tunable laser and photodetector, to excite and interrogate resonances in the press fit microsphere. Figure 4.0.1 shows the setup schematic. The built-in mode-locked fiber ring laser had a $500kHz$ linewidth and $0.25mW$ average power. Sweeping a wavelength range from $1520nm$ to $1570nm$, the repetition rate was set to $5Hz$. Laser light was sent through a three-paddle polarization controller and then a circulator that provided paths to and from the resonator. The detection scheme had $2.5pm$ resolution and a dynamic range $>60dB$.

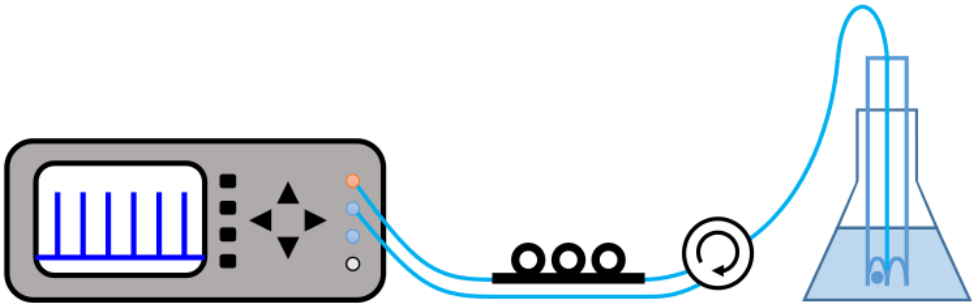

Figure 4.0.1: Setup schematic for interrogating reflection spectra of press fit resonators.

4.1 Reflection spectra

4.1.1 Bow-tie fiber (BTF)

The BTF press fit resonator, when submerged in IPA, shows a mixed reflection spectrum of peaks and dips (Figure 4.1.1(a)). When submerged in DI water, the peaks become reduced while certain dips are enhanced (Figure 4.1.1(b)). An identical range scale in decibels is used for both plots. The peaks and dips in IPA show moderate amplitudes $<5 dB$, whereas the dips in water extend as deep as $7 dB$. The complicated mixed spectrum may be partially attributed to the interruption in the path of circulating WGMs caused the by cladding.

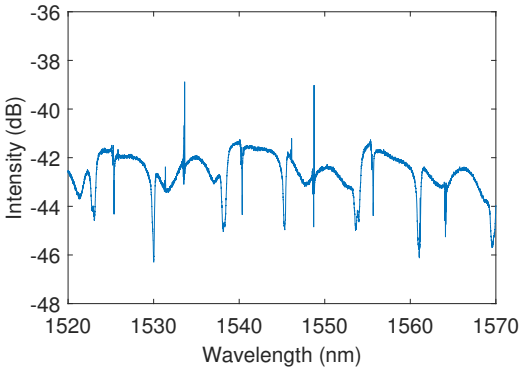

(a) Reflection spectrum in IPA

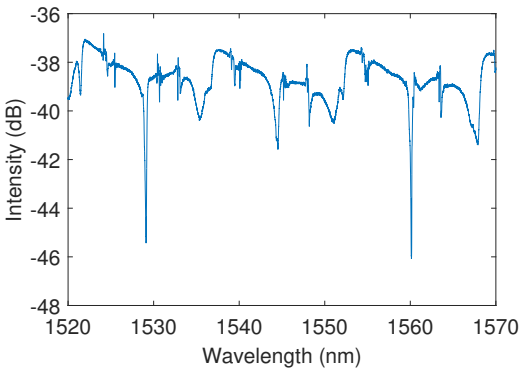

(b) Reflection spectrum in DI water

Figure 4.1.1: Reflection spectra of BTF press fit resonator

4.1.2 Reduced cladding panda fiber (RC-PMF)

In both IPA and DI water, the RC-PMF press fit resonator shows a clean spectrum of well-defined peaks. Carefully note the differing decibel ranges for the spectrum in IPA versus that in water. In IPA the peaks extend as much as $15dB$ above the background (Figure 4.1.2(a)). Then in water, the peaks reach above $20dB$ (Figure 4.1.2(b)). The FSR is easily identified as $13.38nm$. In IPA, the tallest peak located at $1539.12nm$ with width $\Delta\lambda = 15.30pm$ gives a Q factor of 100,600. In DI water, the tallest peak located at $1551.73nm$ with width $\Delta\lambda = 29.02pm$ shows a Q factor of 53,500.

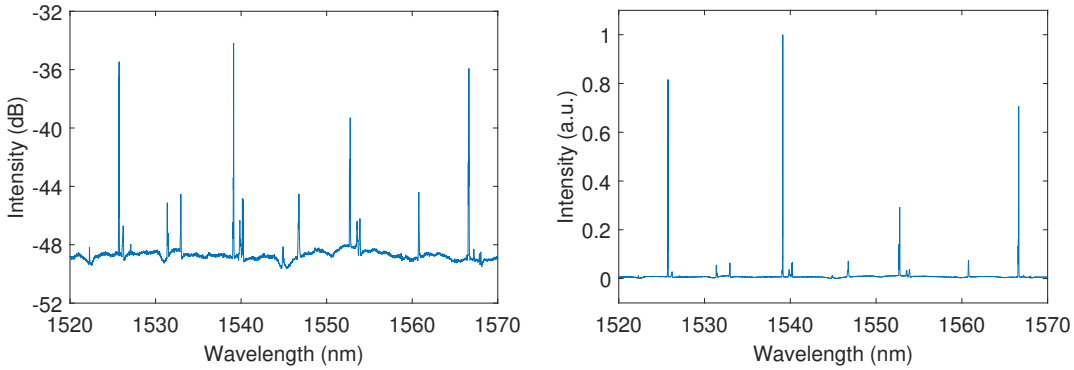

(a) Reflection spectrum in IPA. (left: dB, right: linear)

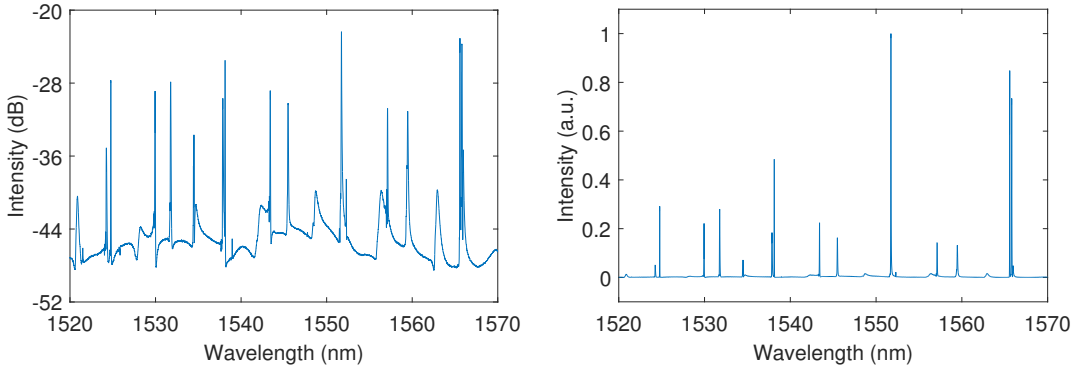

(b) Reflection spectrum in DI water. (left: dB, right: linear)

Figure 4.1.2: Reflection spectra of RC-PMF press fit resonator

4.1.3 Standard cladding panda fiber (SC-PMF)

Just as was seen for the RC-PMF structure, in both IPA and DI water the SC-PMF press fit resonator also shows a clean spectrum of well-defined, quazi-periodic Lorentzian peaks. The same decibel range is presented for each decibel plot. In IPA the peaks extend as much as $17dB$ above the background (Figure 4.1.2(a)). Then in water, the peaks reach up to $12dB$ (Figure 4.1.2(b)). The FSR in IPA is easily found as $7.85nm$. In water, the FSR value is $7.87nm$. These values are

suitable for a ~52μm sphere which makes the spectrum denser than observed for RC-PMF with its ~29μm sphere. In IPA, the peak at 1566.23nm with a width $\Delta\lambda = 63.70pm$ shows a Q factor of 24,600. In DI water, the peak at 1546.35nm has a width $\Delta\lambda = 29.36pm$ for a Q factor of 53,000. Also in DI water, the peak at 1562.33nm with a width $\Delta\lambda = 22.8pm$ yields a Q factor of 69,000. The spectrum in IPA demonstrates a dominant TM mode, while the spectrum in water shows more balanced coupling to TE and TM modes.

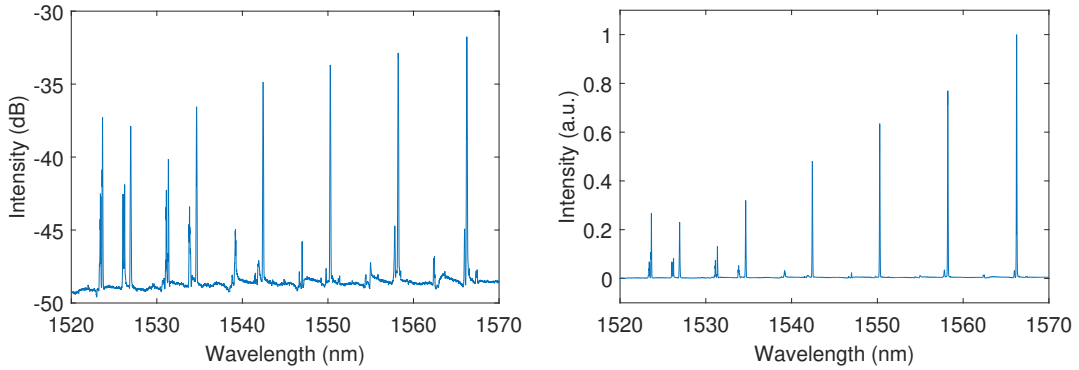

(a) Reflection spectrum in IPA. (left: *dB*, right: linear)

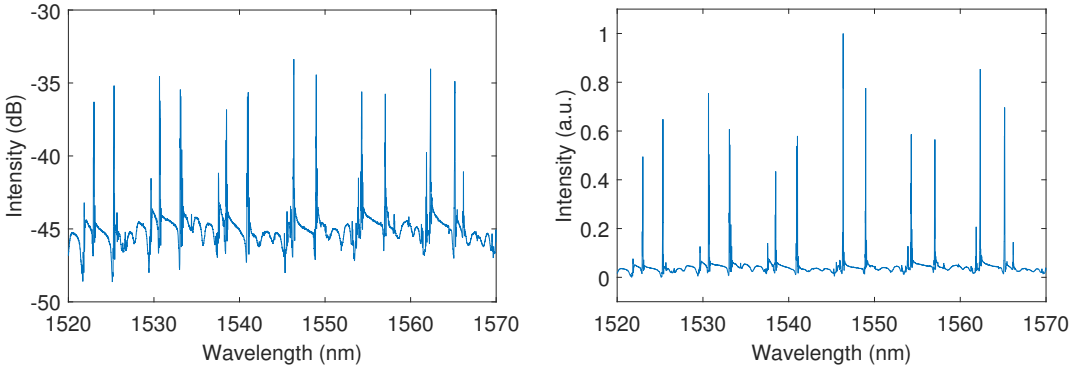

(b) Reflection spectrum in DI water. (left: *dB*, right: linear)

Figure 4.1.3: Reflection spectra of SC-PMF press fit resonator

4.2 Refractive index sensing

Optical refractive index (RI) sensors are widely studied for numerous applications and are already well established in commercialized technologies. A WGM resonator may operate as an RI sensor, since a change in RI of the host medium probed by the resonator causes a corresponding spectral shift of the optical resonance. The resonance shift can then be processed as a sensing signal. For the task of analyzing an unknown liquid sample, the sensor output can be used to determine the RI by comparison with a reference sample. Measurements of RI were performed using an SC-PMF press fit resonator in different concentration solutions of glucose. Glucose was chosen for testing because of its status as the most important simple sugar in human metabolism. An essential carbohydrate, the glucose level in one's body provides an important health indicator that can be interpreted from blood analysis. Glucose in solution demonstrates measurable differences in RI at different concentrations. An experiment was prepared to operate a press fit resonator as an RI sensor and observe its response to different concentrations of glucose in solutions of DI water.

The type of sugar used was D-(+)-glucose, or dextrose. Eleven separate vials were prepared for sugar solutions between 0% and 20% concentration w/w. The assembled press fit resonator was dipped in each test solution and reflection spectra were recorded. In between tests of different sugar solutions, the press

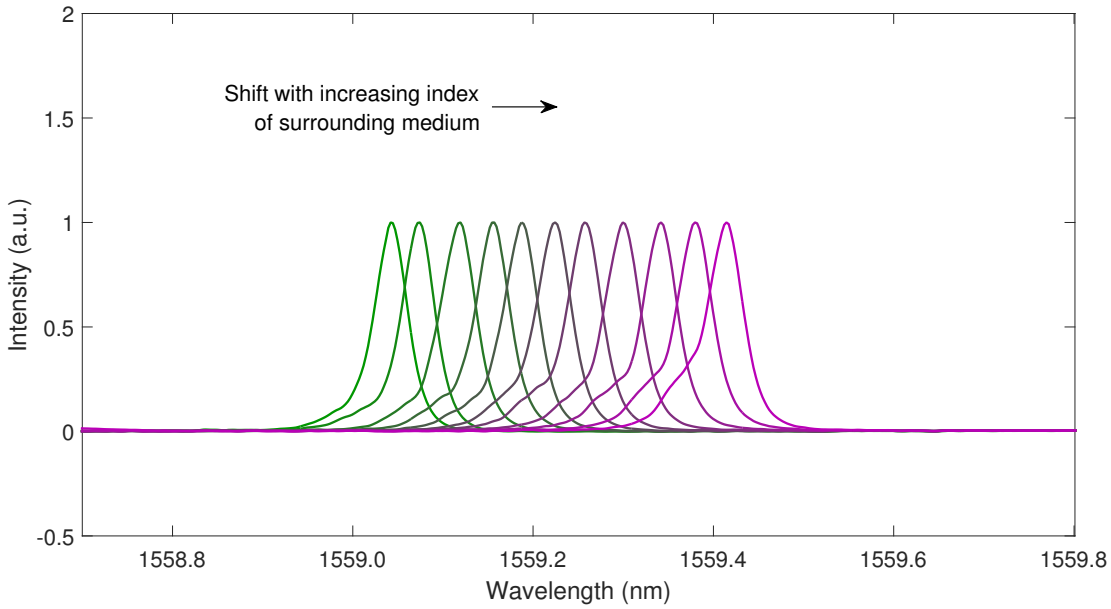

Figure 4.2.1: A WGM resonance shows a red shift toward longer wavelengths for increasing refractive index values of the surrounding medium.

fit resonator was refreshed by stirring in newly obtained DI water. The experiment yielded spectra for eleven discrete sugar solutions. Figure 4.2.1 singles out a resonance peak from the spectrum showing red shifts of the resonance with increasing sugar concentration. Increasing sugar concentration is accompanied by an increasing refractive index of the surrounding medium. The observed shift demonstrates the successful operation of the press fit resonator as an RI sensor. Wavelength tracking of the peak generates another plot characterizing the spectral shift versus sugar concentration. A linear fit with $R^2 = 0.9992$ gives the sensitivity of the press fit resonator as $12.23 nm/RIU$. For a measurement resolution of $2.5 pm$, the detection limit is $2 \times 10^{-4} RIU$.

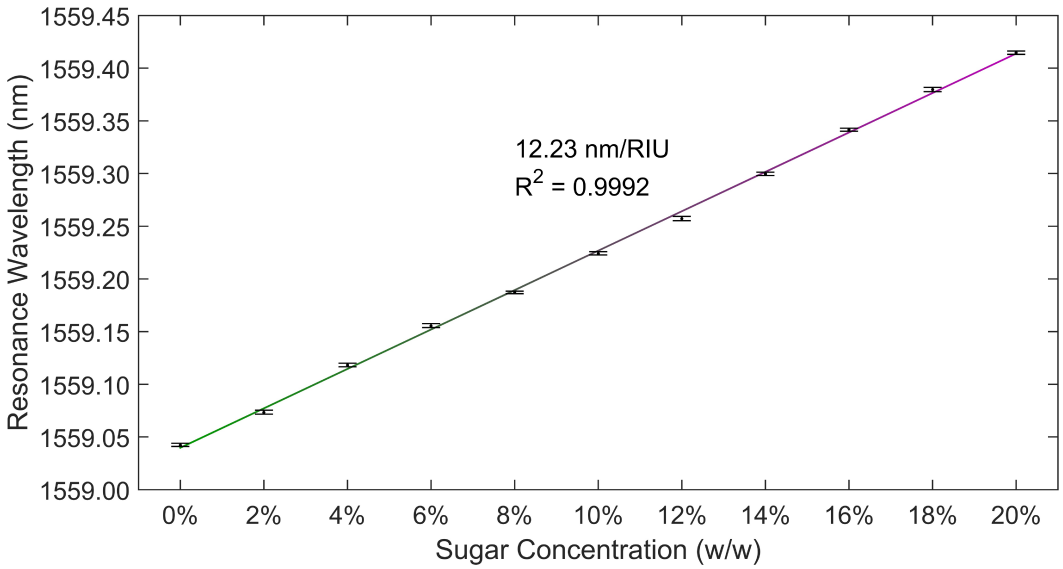

Figure 4.2.2: Resonance wavelength versus sugar concentration is linear in the test range with $R^2 = 0.9992$. The sensitivity is $12.23 nm/RIU$.

4.3 Temperature cross-sensitivity

If left uncompensated, spectral shifts due to temperature fluctuations may induce false positive detections of bio-analytes. Sensors are typically calibrated by simultaneously recording the temperature in the medium. For biosensing, it is especially crucial to monitor temperature when introducing the analyte into the water-filled chamber surrounding the sensor. Temperature disparities between the water in the chamber and the added analyte will induce a shift in the measured signal as the temperature reaches equilibrium. Only by compensating temperature-induced spectral shifts can the sensor output be properly interpreted. In practice, it is advantageous that the temperature cross-sensitivity be small and linear within the range of operation.

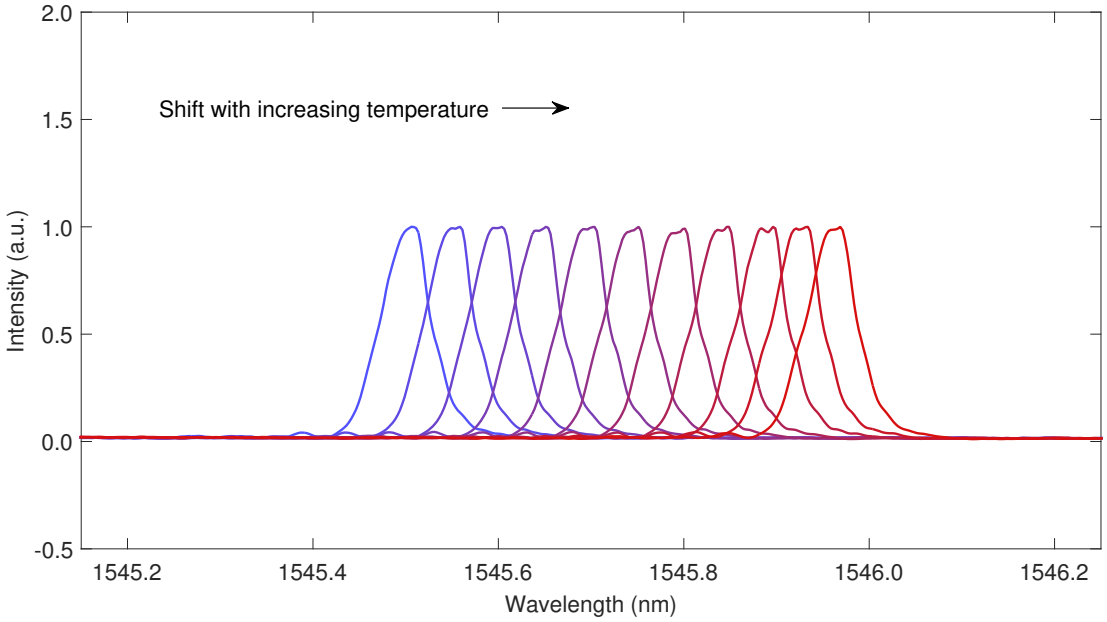

Figure 4.3.1: Peak tracking of a WGM resonance shows a red shift toward longer wavelengths for increasing temperature.

To test the temperature cross-sensitivity of the press fit resonator, an SC-PMF variety was prepared. The sensor, submersed in a water-filled flask, was placed inside an environmental test chamber (TestEquity 1000 Series). The test chamber, provides both chilling and heating capabilities, with a prescribed temperature accuracy $\pm 0.1°C$. The reflection spectrum in DI water was monitored for controlled temperature conditions (Figure 4.3.1). Starting from room temperature (25°C), the chamber was chilled down to 10°C at a rate of $-0.5°C/min$. Temperature setpoints were chosen for every 5°C between 10°C and 60°C. The test chamber was programmed to maintain temperature for two hours at every setpoint to allow the water surrounding the sensor to reach thermal equilibrium. Between setpoints, the test chamber was heated at a rate of $+0.5°C/min$. Finishing at 60°C, the

chamber was cooled at a rate of $-1°C/min$ back down to room temperature.

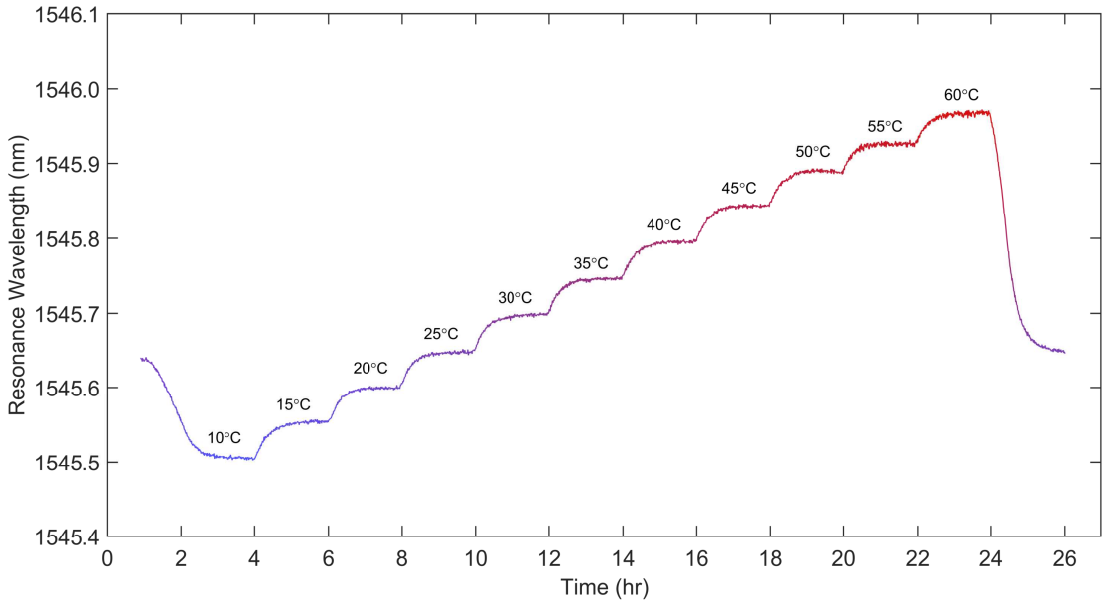

Figure 4.3.2: Resonance wavelength is tracked versus temperature for an SC-PMF press fit resonator in water. The test chamber temperature was controlled through a 50°C range in steps of 5°C. The sensor was chilled down to 10°C, then heated up to 60°C. A staircase pattern is observed because of the two hour dwell time at each temperature setpoint.

The duration of the measurement was nearly 26 hours. During the course of the measurement, twenty reflection spectra from the sensor were recorded every $30sec$. Peak tracking was performed to yield a plot of resonance wavelength versus time (Figure 4.3.2). Each point in the plot represents the mean of twenty spectra. The staircase pattern at two hour intervals well matches the chosen duration and ramping between temperature setpoints. Explicit labels identify particular setpoints in the range between 10°C and 60°C. The plateau of each step represents when the temperature of the water has reached thermal equilibrium with the

rest of the test chamber. The resonance wavelength extracted from each plateau provides information to plot resonance wavelength versus temperature. Resonant wavelength versus temperature demonstrates excellent linearity in the test range giving $R^2 = 0.9991$. The temperature cross-sensitivity is calculated as $9.4pm/°\text{C}$. For a measurement resolution of $2.5pm$, the detection limit is 0.3°C.

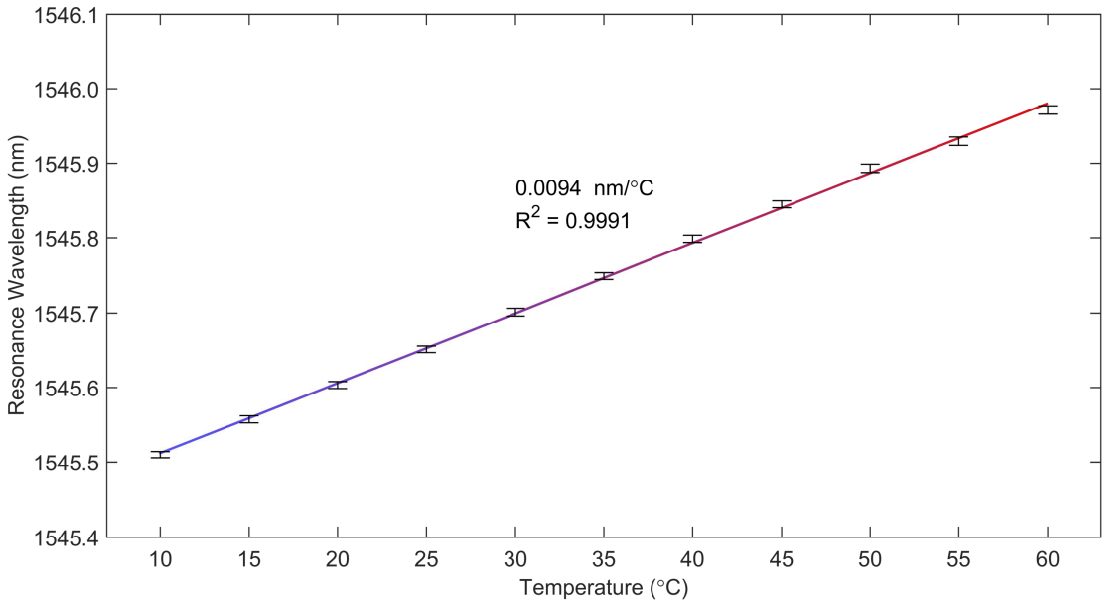

Figure 4.3.3: Resonance wavelength versus temperature is linear in the test range with $R^2 = 0.9991$. The temperature cross-sensitivity is $9.4pm/°\text{C}$

Chapter 5

Conclusions & future work

This dissertation detailed the design and realization of optical fiber microstructures for self-contained excitation of whispering gallery modes. The fabrication and function of three novel press fit spherical resonators were demonstrated. Etching methods were developed using standard etchants on common polarization-maintaining fiber. Quick and repeatable, the procedures for etching and assembly are amenable to mass production. The final structures are compact and robust, enabling coupling to WGMs in a portable, integrated fiber-optic platform. Alignment-free coupling and secure storage of a microsphere is achieved together with efficient excitation and interrogation of WGMs.

The pigtailed format of the device lends a convenience and ease to measurements with WGMs, which makes it very attractive for sensing applications. Refractive index sensing was initially demonstrated by monitoring the resonance shift of the press fit resonator in different concentrations of glucose solution. The

present design can be modified for various bioscience sensing tasks by applying a coating that maximizes adsorption of a desired chemical or biomolecule to the BTO sphere. The incorporation of different types of spheres is imagined for different applications. A rare earth doped sphere could be integrated to produce a laser. A porous sphere could be used to fabricate an ultra-compact gas cell that leverages the long interaction length of circulating WGMs to perform spectroscopy. A hollow sphere could be applied to create a medical diagnostic probe for accurate pressure readings during surgery. Another avenue for the curious would be an investigation of resonant bispheres for filter applications or fundamental studies. An achievable bisphere arrangement is shown in Figure 5.0.1 for the SC-PMF press fit structure.

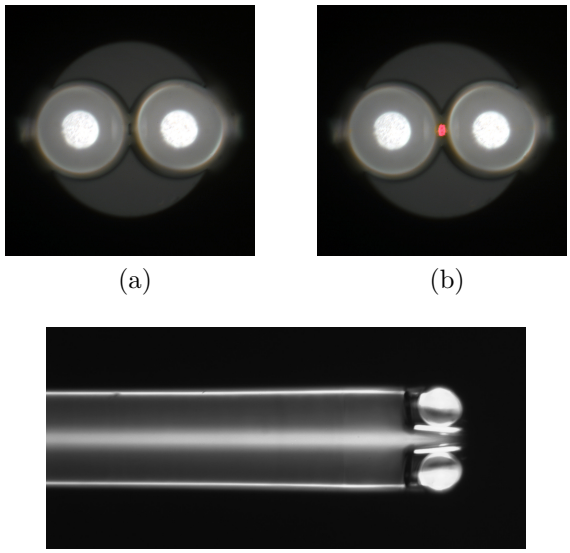

(a) (b)

(c)

Figure 5.0.1: Microscope images of a press fit bisphere resonator. (a) End-face view. (b) End-face view with taper excitation by He-Ne laser. (c) Side view.

Bibliography

[1] Lord Rayleigh. The problem of the whispering gallery. *The London, Edinburgh, and Dublin Philosophical Magazine and Journal of Science*, 20(120):1001–1004, 1910.

[2] Lord Rayleigh. Further applications of Bessel's functions of high order to the Whispering Gallery and allied problems. *The London, Edinburgh, and Dublin Philosophical Magazine and Journal of Science*, 27(157):100–109, 1914.

[3] John William Strutt Rayleigh and Robert Bruce Lindsay. *The theory of sound*. Dover, New York, 2d ed., rev. and enl. edition, 1945.

[4] Ming Cai and Kerry Vahala. Highly efficient hybrid fiber taper coupled microsphere laser. *Optics Letters*, 26(12):884 – 886, June 2001.

[5] M. Cai, O. Painter, K. J. Vahala, and P. C. Sercel. Fiber-coupled microsphere laser. *Optics Letters*, 25(19):1430 – 1432, October 2000.

[6] B.E Little, S.T Chu, H.A Haus, J Foresi, and J.-P Laine. Microring resonator channel dropping filters. *Journal of Lightwave Technology*, 15(6):998 – 1005, 1997.

[7] F. C. Blom, D. R. van Dijk, H. J. W. M. Hoekstra, A. Driessen, and Th J. A. Popma. Experimental study of integrated-optics microcavity resonators: Toward an all-optical switching device. *Applied physics letters*, 71(6):747 – 749, 1997.

[8] R. W. Boyd and J. E. Heebner. Sensitive disk resonator photonic biosensor. *Applied optics*, 40(31):5742, November 2001.

[9] Martin Baaske and Frank Vollmer. Optical Resonator Biosensors: Molecular Diagnostic and Nanoparticle Detection on an Integrated Platform. *ChemPhysChem*, 13(2):427–436, February 2012.

[10] C. G. B Garrett, W Kaiser, and W. L Bond. Stimulated Emission into Optical Whispering Modes of Spheres. *Physical Review*, 124(6):1807 – 1809, December 1961.

[11] L. F. Stokes, M. Chodorow, and H. J. Shaw. All-single-mode fiber resonator. *Optics Letters*, 7(6):288 – 290, June 1982.

[12] V. B. Braginsky and V. S. Chenko. Properties of optical dielectric microresonators. In *Soviet Physics Doklady*, volume 32, page 306, 1987.

[13] V. B. Braginsky, M. L. Gorodetsky, and V. S. Ilchenko. Quality-factor and nonlinear properties of optical whispering-gallery modes. *Physics Letters A*, 137(7):393–397, May 1989.

[14] M. L. Gorodetsky, A. A. Savchenkov, and V. S. Ilchenko. Ultimate Q of optical microsphere resonators. *Optics Letters*, 21(7):453 – 455, April 1996.

[15] SL McCall, AFJ Levi, RE Slusher, SJ Pearton, and RA Logan. Whispering-gallery mode microdisk lasers. *Applied Physics Letters*, 60(3):289 – 291, January 1992.

[16] Y. Yamamoto and RE Slusher. Optical processes in microcavities. *Physics Today*, 46(6):66 – 73, June 1993.

[17] JP Zhang, DY Chu, SL Wu, ST Ho, WG Bi, CW Tu, and RC Tiberio. Photonic-wire laser. *Physical Review Letters*, 75(14):2678 – 2681, October 1995.

[18] J.P Zhang, D.Y Chu, S.L Wu, W.G Bi, R.C Tiberio, C.W Tu, and S.T Ho. Directional light output from photonic-wire microcavity semiconductor lasers. *IEEE Photonics Technology Letters*, 8(8):968 – 970, 1996.

[19] D. K. Armani, T. J. Kippenberg, S. M. Spillane, and K. J. Vahala. Ultra-high-Q toroid microcavity on a chip. *Nature*, 421(6926):925–928, February 2003.

[20] B. K. Min, T. J. Kippenberg, L. Yang, K. J. Vahala, J. Kalkman, and A. Polman. Erbium-implanted high-Q silica toroidal microcavity laser on a silicon chip. *PHYSICAL REVIEW A*, 70(3):12, September 2004.

[21] T. J. Kippenberg, S. M. Spillane, D. K. Armani, and K. J. Vahala. Ultralow-threshold microcavity Raman laser on a microelectronic chip. *Optics Letters*, 29(11):1224 – 1226, June 2004.

[22] S. M Spillane, T. J Kippenberg, and K. J Vahala. Ultralow-threshold Raman laser using a spherical dielectric microcavity. *Nature*, 415(6872):621 – 623, February 2002.

[23] J. W. Hall and A. Pollard. Near-infrared spectrophotometry: a new dimension in clinical chemistry. *Clinical Chemistry*, 38(9):1623 – 1631, September 1992.

[24] S Blair and Y Chen. Resonant-enhanced evanescent-wave fluorescence biosensing with cylindrical optical cavities. *Applied Optics*, 40(4):570, February 2001.

[25] R. W Boyd, J. E Heebner, N. N Lepeshkin, Q.-H Park, A Schweinsberg, G. W Wicks, A. S Baca, J. E Fajardo, R. R Hancock, M. A Lewis, R. M Boysel, M Quesada, R Welty, A. R Bleier, J Treichler, and R. E Slusher. Nanofabrication of optical structures and devices for photonics and biophotonics. *Journal of Modern Optics*, 50(15):2543 – 2550, October 2003.

[26] F. Vollmer, D. Braun, A. Libchaber, M. Khoshsima, I. Teraoka, and S. Arnold. Protein detection by optical shift of a resonant microcavity. *Applied Physics Letters*, 80(21):4057–4059, May 2002.

[27] Frank Vollmer and Stephen Arnold. Whispering-gallery-mode biosensing: label-free detection down to single molecules. *Nature Methods*, 5(7):591–596, July 2008.

[28] S. Arnold, M. Khoshsima, I. Teraoka, S. Holler, and F. Vollmer. Shift of whispering-gallery modes in microspheres by protein adsorption. *Optics Letters*, 28(4):272, February 2003.

[29] Iwao Teraoka, Stephen Arnold, and Frank Vollmer. Perturbation approach to resonance shifts of whispering-gallery modes in a dielectric microsphere as a probe of a surrounding medium. *Journal of the Optical Society of America B*, 20(9):1937, 2003.

[30] Iwao Teraoka and Stephen Arnold. Theory of resonance shifts in TE and TM whispering gallery modes by nonradial perturbations for sensing applications. *Journal of the Optical Society of America B*, 23(7):1381, 2006.

[31] Iwao Teraoka and Stephen Arnold. Resonance shifts of counterpropagating whispering-gallery modes: degenerate perturbation theory and application to resonator sensors with axial symmetry. *Journal of the Optical Society of America B*, 26(7):1321, July 2009.

[32] Frank Vollmer, Stephen Arnold, Dieter Braun, Iwao Teraoka, and Albert Libchaber. Multiplexed DNA Quantification by Spectroscopic Shift of Two Microsphere Cavities. *Biophysical Journal*, 85(3):1974–1979, September 2003.

[33] Rasheeda M. Hawk, Maria V. Chistiakova, and Andrea M. Armani. Monitoring DNA hybridization using optical microcavities. *Optics Letters*, 38(22):4690, November 2013.

[34] Mohammed Sharif Murib, Weng-Siang Yeap, Daan Martens, Peter Bienstman, Ward De Ceuninck, Bart van Grinsven, Michael J. Schöning, Luc Michiels, Ken Haenen, Marcel Ameloot, Ali Serpengüzel, and Patrick Wagner. Photonic detection and characterization of DNA using sapphire microspheres. *Journal of Biomedical Optics*, 19(9):097006–097006, 2014.

[35] Jonathan D. Suter, Ian M. White, Hongying Zhu, Huidong Shi, Charles W. Caldwell, and Xudong Fan. Label-free quantitative DNA detection using the liquid core optical ring resonator. *Biosensors and Bioelectronics*, 23(7):1003–1009, February 2008.

[36] F. Vollmer, S. Arnold, and D. Keng. Single virus detection from the reactive shift of a whispering-gallery mode. *Proceedings of the National Academy of Sciences*, 105(52):20701–20704, December 2008.

[37] Melinda S. McClellan, Leslie L. Domier, and Ryan C. Bailey. Label-free virus detection using silicon photonic microring resonators. *Biosensors and Bioelectronics*, 31(1):388–392, January 2012.

[38] Adam L Washburn and Ryan C Bailey. Photonics-on-a-chip: recent advances in integrated waveguides as enabling detection elements for real-world, lab-

on-a-chip biosensing applications. *ANALYST*, 136(2):227 – 236, December 2010.

[39] Andrea Armani, Carol Soteropulos, and Heather Hunt. Determination of binding kinetics using whispering gallery mode microcavities. *Applied Physics Letters*, 99(10):103703 – 103703–3, September 2011.

[40] K. A. Wilson, C. A. Finch, P. Anderson, F. Vollmer, and J. J. Hickman. Whispering gallery mode biosensor quantification of fibronectin adsorption kinetics onto alkylsilane monolayers and interpretation of resultant cellular response. *BIOMATERIALS*, 33(1):225 – 236, January 2012.

[41] Matthew R. Foreman and Frank Vollmer. Optical Tracking of Anomalous Diffusion Kinetics in Polymer Microspheres. *Physical Review Letters*, 114(11):118001, March 2015.

[42] D. W. Vernooy, A. Furusawa, N. Ph. Georgiades, V. S. Ilchenko, and H. J. Kimble. Cavity QED with high-Q whispering gallery modes. *Physical Review A*, 57(4):R2293–R2296, April 1998.

[43] Young-Shin Park, Andrew K. Cook, and Hailin Wang. Cavity QED with Diamond Nanocrystals and Silica Microspheres. *Nano Letters*, 6(9):2075–2079, September 2006.

[44] G. Anetsberger, O. Arcizet, Q. P. Unterreithmeier, R. Rivière, A. Schliesser, E. M. Weig, J. P. Kotthaus, and T. J. Kippenberg. Near-field cavity optomechanics with nanomechanical oscillators. *Nature Physics*, 5(12):909–914, December 2009.

[45] L. M. Baumgartel, R. J. Thompson, and N. Yu. Frequency stability of a dual-mode whispering gallery mode optical reference cavity. *Optics Express*, 20(28):29798, December 2012.

[46] J. Alnis, A. Schliesser, C. Y. Wang, J. Hofer, T. J. Kippenberg, and T. W. Hänsch. Thermal-noise-limited crystalline whispering-gallery-mode resonator for laser stabilization. *Physical Review A*, 84(1):011804, July 2011.

[47] V. Sandoghdar, F. Treussart, J. Hare, V. Lefèvre-Seguin, J. M. Raimond, and S. Haroche. Very low threshold whispering-gallery-mode microsphere laser. *Physical Review A*, 54(3):R1777–R1780, September 1996.

[48] Valérie Lefèvre-Seguin. Whispering-gallery mode lasers with doped silica microspheres. *Optical Materials*, 11(2–3):153–165, January 1999.

[49] V.S. Ilchenko and A.B. Matsko. Optical resonators with whispering-gallery modes-part II: applications. *IEEE Journal of Selected Topics in Quantum Electronics*, 12(1):15–32, January 2006.

[50] R. J. Thompson, Q. A. Turchette, O. Carnal, and H. J. Kimble. Nonlinear spectroscopy in the strong-coupling regime of cavity QED. *Physical Review A*, 57(4):3084–3104, April 1998.

[51] Kristopher J. Rowland, Alexandre François, and Tanya M. Monro. Excitation and lasing of whispering gallery modes in dye doped microspheres at the tip of a microstructured optical fiber and application for a sensitive dip sensor architecture. In *SPIE BiOS*, pages 82180M–82180M. International Society for Optics and Photonics, 2012.

[52] Silvia Soria, Simone Berneschi, Massimo Brenci, Franco Cosi, Gualtiero Nunzi Conti, Stefano Pelli, and Giancarlo C. Righini. Optical Microspherical Resonators for Biomedical Sensing. *Sensors*, 11(12):785–805, January 2011.

[53] Niranjan M. Hanumegowda, Caleb J. Stica, Bijal C. Patel, Ian White, and Xudong Fan. Refractometric sensors based on microsphere resonators. *Applied Physics Letters*, 87(20):201107, November 2005.

[54] Michael Himmelhaus, Sivashankar Krishnamoorthy, and Alexandre Francois. Optical Sensors Based on Whispering Gallery Modes in Fluorescent Microbeads: Response to Specific Interactions. *Sensors*, 10(6):6257–6274, 2010.

[55] Tindaro Ioppolo, Ulas Ayaz, and M. Volkan Ötügen. Tuning of whispering gallery modes of spherical resonators using an external electric field. *Optics Express*, 17(19):16465, September 2009.

[56] S. Avino, C. Richmond, A. Giorgini, P. Malara, R. Zullo, P. De Natale, and G. Gagliardi. High-sensitivity ring-down evanescent-wave sensing in fiber resonators. *Optics Letters*, 39(19):5725, October 2014.

[57] Vladimir S. Ilchenko, X. Steve Yao, and Lute Maleki. Pigtailing the high-Q microsphere cavity: a simple fiber coupler for optical whispering-gallery modes. *Optics Letters*, 24(11):723 – 725, June 1999.

[58] A. Serpengüzel, S. Arnold, G. Griffel, and J. A. Lock. Enhanced coupling to microsphere resonances with optical fibers. *Journal of the Optical Society of America B*, 14(4):790 – 795, April 1997.

[59] A. Serpengüzel, S. Arnold, and G. Griffel. Excitation of resonances of microspheres on an optical fiber. *Optics Letters*, 20(7):654 – 656, April 1995.

[60] Ming Cai, Oskar Painter, and Kerry J. Vahala. Observation of critical coupling in a fiber taper to a silica-microsphere whispering-gallery mode system. *Physical review letters*, 85(1):74, 2000.

[61] J. C. Knight, G. Cheung, F. Jacques, and T. A. Birks. Phase-matched excitation of whispering-gallery-mode resonances by a fiber taper. *Optics Letters*, 22(15):1129 – 1131, August 1997.

[62] L. Arques, A. Carrascosa, V. Zamora, A. Díez, J. L. Cruz, and M. V. Andrés. Excitation and interrogation of whispering-gallery modes in optical microresonators using a single fused-tapered fiber tip. *Optics Letters*, 36(17):3452, September 2011.

[63] Kyriaki Kosma, Gianluigi Zito, Kay Schuster, and Stavros Pissadakis. Whispering gallery mode microsphere resonator integrated inside a microstructured optical fiber. *Optics Letters*, 38(8):1301, April 2013.

[64] Alexandre François, Kristopher J. Rowland, and Tanya M. Monro. Highly efficient excitation and detection of whispering gallery modes in a dye-doped microsphere using a microstructured optical fiber. *Applied Physics Letters*, 99(14):141111, October 2011.

[65] Hanzheng Wang, Xinwei Lan, Jie Huang, Lei Yuan, Cheol-Woon Kim, and Hai Xiao. Fiber pigtailed thin wall capillary coupler for excitation of microsphere WGM resonator. *Optics Express*, 21(13):15834, July 2013.

[66] Ruohui Wang, Michael Fraser, Jiacheng Li, Xueguang Qiao, and Anbo Wang. Integrated in-fiber coupler for microsphere whispering-gallery modes resonator excitation. *Optics Letters*, 40(3):308, February 2015.

[67] C. H. Townes and A. L. Schawlow. *Microwave Spectroscopy*. Courier Corporation, October 2013.

[68] A.B. Matsko and V.S. Ilchenko. Optical resonators with whispering-gallery modes-part I: basics. *IEEE Journal of Selected Topics in Quantum Electronics*, 12(1):3–14, January 2006.

[69] Andrey B. Matsko. *Practical applications of microresonators in optics and photonics*, volume 146. of *Optical science and engineering*. CRC Press, Boca Raton, 2009.

[70] R. Ulrich. Theory of the Prism-Film Coupler by Plane-Wave Analysis. *Journal of the Optical Society of America*, 60(10):1337, October 1970.

[71] Dror Sarid. High efficiency input–output prism waveguide coupler: an analysis. *Applied Optics*, 18(17):2921, September 1979.

[72] P. K. Tien and R. Ulrich. Theory of prism-film coupler and thin-film light guides. *JOSA*, 60(10):1325–1337, 1970.

[73] M. L. Gorodetsky and V. S. Ilchenko. High-Q optical whispering-gallery microresonators: precession approach for spherical mode analysis and emission patterns with prism couplers. *Optics Communications*, 113(1–3):133–143, December 1994.

[74] Yong-Le Pan and Richard K. Chang. Highly efficient prism coupling to whispering gallery modes of a square μ cavity. *Applied Physics Letters*, 82(4):487–489, January 2003.

[75] M. L. Gorodetsky and V. S. Ilchenko. Optical microsphere resonators: optimal coupling to high-Q whispering-gallery modes. *Journal of the Optical Society of America B*, 16(1):147, January 1999.

[76] Robert H. Webb. *Elementary wave optics*. Academic Press, New York, 1969.

[77] Peter W. Barber and Richard Kounai Chang. *Optical effects associated with small particles*, volume 1. World Scientific, 1988.

[78] E. James Davis and Gustav Schweiger. *The airborne microparticle: its physics, chemistry, optics, and transport phenomena*. Springer, New York, 2002.

[79] R. R. A. Syms and J. R. Cozens. *Optical guided waves and devices*. McGraw-Hill, New York, 1992.

[80] Motoichi Ohtsu and K. Kobayashi. *Optical near fields: introduction to classical and quantum theories of electromagnetic phenomena at the nanoscale*. Advanced texts in physics. Springer, Berlin ; New York, 2004.

[81] Gustav Mie. Beiträge zur Optik trüber Medien, speziell kolloidaler Metallösungen. *Annalen der Physik*, 330(3):377–445, January 1908.

[82] Julius Adams Stratton. *Electromagnetic theory*. John Wiley & Sons, 2007.

[83] Craig F. Bohren and Donald R. Huffman. *Absorption and scattering of light by small particles*. John Wiley & Sons, 2008.

[84] H. C. van de Hulst. *Light scattering by small particles*. Structure of matter series. Wiley, New York, 1957.

[85] Milton Kerker. *The Scattering of Light and Other Electromagnetic Radiation: Physical Chemistry: A Series of Monographs*. Academic Press, October 2013.

[86] Michael Quinten. *Optical properties of nanoparticle systems: Mie and beyond*. Wiley-VCH, Weinheim, 2011.

[87] Walter T. Grandy Jr and Walter T. Grandy. *Scattering of waves from large spheres*. Cambridge University Press, 2005.

[88] Barbara J. Messinger, K. Ulrich von Raben, Richard K. Chang, and Peter W. Barber. Local fields at the surface of noble-metal microspheres. *Physical Review B*, 24(2):649–657, July 1981.

[89] Herman Chew, Dau-Sing Wang, and Milton Kerker. Elastic scattering of evanescent electromagnetic waves. *Applied Optics*, 18(15):2679 – 2687, August 1979.

[90] C Liu, T Kaiser, S Lange, and G Schweiger. Structural resonances in a dielectric sphere illuminated by an evanescent wave. *Optics Communications*, 117(5):521 – 531, 1995.

[91] M. Quinten, A. Pack, and R. Wannemacher. Scattering and extinction of evanescent waves by small particles. *Applied Physics B*, 68(1):87–92, January 1999.

[92] Motoichi Ohtsu and Hirokazu Hori. *Near-field nano-optics: from basic principles to nano-fabrication and nano-photonics*. Lasers, photonics, and electro-optics. Kluwer/Plenum Publishers, New York, 1999.

[93] A. Klini, T. David, E. Bourillot, S. Emonin, P. Papadopoulos, J. P. Goudonnet, and G. Kotrotsios. Reproducible optical fiber tips for photon scanning tunneling microscopy with very small (<5°) cone angle. *Journal of Lightwave Technology*, 16(7):1220–1227, July 1998.

Appendix A

Mie angular functions

Mie theory commonly defines two important angular-dependent functions $\Pi_{l,m}$ and $\tau_{l,m}$ as

$$\Pi_{l,m}(\theta) = m\frac{P_l^m(\cos\theta)}{\sin\theta} \tag{A.0.1}$$

$$\tau_{l,m}(\theta) = \frac{dP_l^m(\cos\theta)}{d\theta} \tag{A.0.2}$$

In the plane wave case, $m = 1$, the functions become

$$\Pi_{l,1}(\theta) = \frac{P_l^1(\cos\theta)}{\sin\theta} \tag{A.0.3}$$

$$\tau_{l,1}(\theta) = \frac{dP_l^1(\cos\theta)}{d\theta} \tag{A.0.4}$$

Using abbreviations in notation, they are

$$\Pi_l = \Pi_{l,1} \tag{A.0.5}$$

$$\tau_l = \tau_{l,1} \tag{A.0.6}$$

Figure A.0.1 depicts the the angular dependence of these functions for orders $l = 1, 2, 3$, and 4.

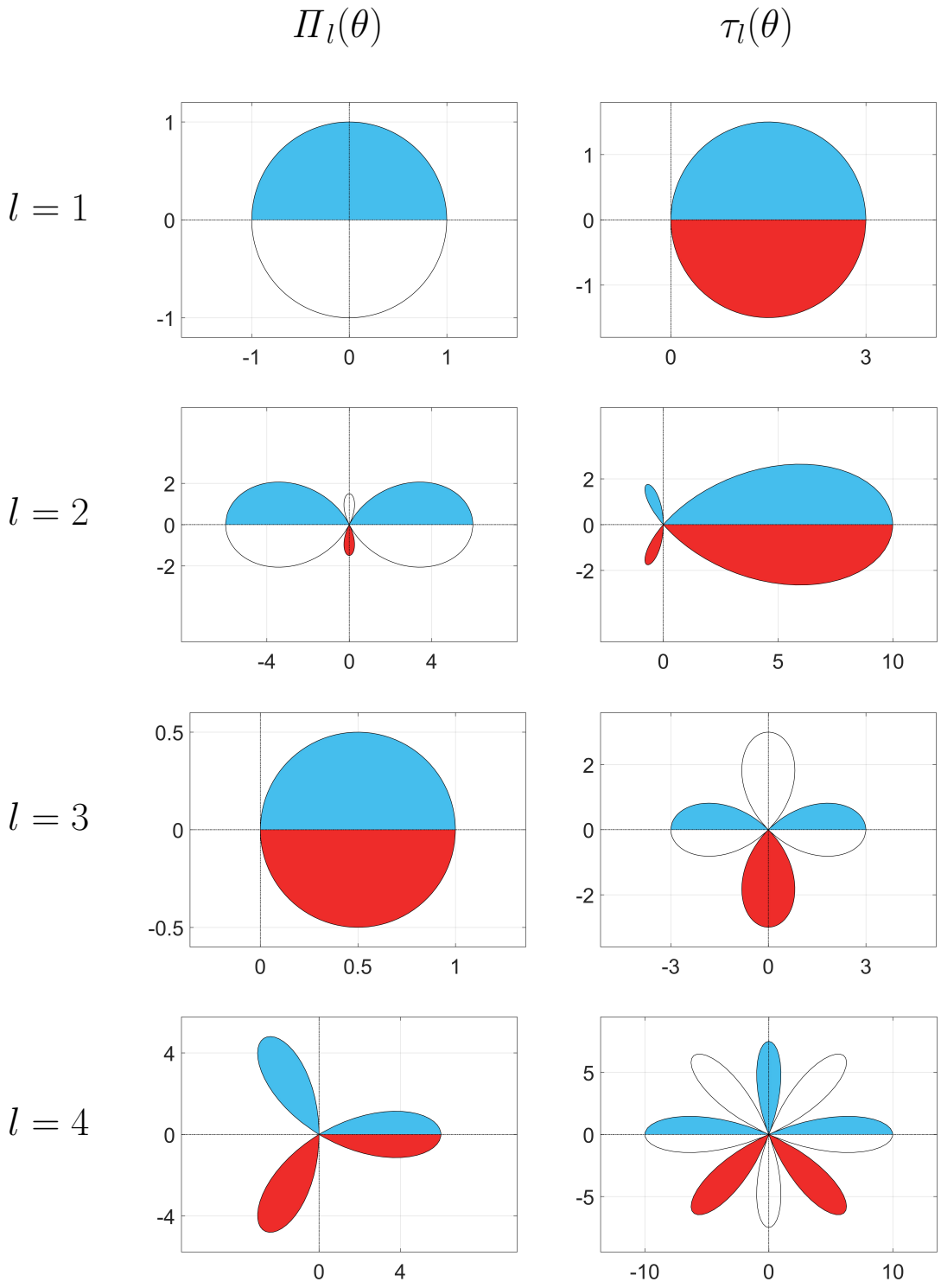

Figure A.0.1: Mie angular functions $\Pi_l(\theta)$ and $\tau_l(\theta)$ are shown in polar plots over the interval $[0, 2\pi]$. Colors indicate the sign of the function for $\theta \in [0, \pi]$ where blue and red are positive and negative, respectively.

Appendix B

Other candidate resonator designs

Shown in Figure B.0.1 are many other candidate designs for in-fiber WGM resonators that were considered and attempted, but were not fully described in this dissertation. These other designs featured both etching and splicing procedures on various fiber types that resulted in either end-fire or tangential optical excitation of a sphere. However, the press fit resonators presented were the best of all in terms of ease of fabrication, reproducibility, and performance.

Figure B.0.1: Other candidate designs for in-fiber WGM resonators.